JOURNAL OF GEOPHYSICAL RESEARCH, VOL. 101, NO. B12, PAGES 27,957-27,980, DECEMBER 10, 1996

Crustal deformation across and beyond the Los Angeles basin from geodetic measurements

Zheng-Kang Shen, David D. Jackson, and Bob X. Ge

Department of Earth and Space Sciences, University of California, Los Angeles

Abstract. We combine 6 years of Global Positioning System (GPS) data with 20 years of trilateration data and a century of triangulation, taped distance, and astronomic azimuth measurements to derive 66 interseismic station velocities in the greater Los Angeles region. We interpolate the velocities to construct a regional strain rate map beyond the Los Angeles basin. Our results generally agree with the model proposed by the Working Group on California Earthquake Probabilities in 1995. Important regional findings of this study are as follows: (1) There is a significant N-S convergence and E-W extension, about 0.22 and 0.17 $\pm$ 0.05 μstrain/yr, respectively, for the two components, along the southern frontal fault system of the San Gabriel Mountains. (2) The crustal deformation around the Big Bend of the San Andreas fault (SAF) cannot be explained solely by wrench-style motion across the SAF. Remaining motion could be part of a NW-SE extension which is the response to NE-SW compression in the central Transverse Ranges region. Alternatively, it could be caused by left-lateral faulting on an oblique blind thrust beneath the San Gabriel Mountains. (3) Low strain rates are found along the Elsinore fault and Newport-Inglewood fault. (4) North-south compression decreases from the Raymond Hill fault westward to the Santa Monica fault. There is little east-west extension along this fault system.

Introduction

The greater Los Angeles region continues to challenge the research community because it is tectonically complex and subject to perilous seismic hazards. Geological studies show the Los Angeles basin to be a deep sedimentary basin at the junction of the northern Peninsular Ranges and the central Transverse Ranges. Formation of the basin started during Miocene time [*Wright*, 1987] through a pull-apart process. Five million years ago, the opening Gulf of California migrated the boundary between the Pacific and the North America plates to the San Andreas fault (SAF) east of the basin and created a left step, known as the Big Bend, along a right-lateral strike-slip SAF north and east of the basin [*Atwater*, 1989]. The region started to undergo compression as it moved NW toward the Big Bend. Evolution of the basin involved volcanism, uplift, extension, block rotation, pulling apart, shear faulting, compression, and folding [*Campbell and Yerkes*, 1976; *Wright*, 1987]. At present, the sediments in the central basin are more than 10 km thick, forming a northwest-southeast elongated synclinorium, with its flanks folded and cut by a group of Quaternary active faults [*Ziony and Yerkes*, 1985].

Paper number 96JB02544.
0148-0227/96/96JB-02544$09.00

South of the basin, present-day crustal deformation is dominated by NW trending strike slip faults such as the SAF, the San Jacinto fault (SJF), the Elsinore fault, and the Newport-Inglewood fault. The SJF merges with the SAF east of the basin. The Whittier-Elsinore fault system, the Newport-Inglewood fault, and the Palos Verdes fault cut through the east and west flanks of the basin [*Ziony and Yerkes*, 1985] (Figure 1). North of the basin, the San Gabriel Mountains have been pushed up by a frontal thrust fault system defined by the Sierra Madre-Cucamonga fault system along the SE and the Santa Susana fault along the SW. The E-W trending Malibu-Santa Monica-Raymond Hill fault system uplifted the Santa Monica Mountains [*Davis et al.*, 1989]. Horizontal detachment in the lower crust or at the Moho boundary has been suggested beneath most of the central and western Transverse Ranges [*Bird and Rosenstock*, 1984; *Weldon and Humphreys*, 1986; *Namson and Davis*, 1988]. Furthermore, such thrust and horizontal detachment in the Los Angeles basin region have been identified by recent geomorphological and trenching studies [*Dolan et al.*, 1995; *Huftile and Yeats*, 1995].

Earthquakes also help illuminate the tectonics of the Los Angeles basin. Earthquake focal mechanisms show a mixture of NW dextral strike slip and N-S convergence [*Hauksson*, 1990]. Earthquakes of right-lateral strike-slip faulting represented by the 1933 M 6.4 Long Beach earthquake dominate the seismicity south of the basin. (Throughout this paper, M represents moment magni-

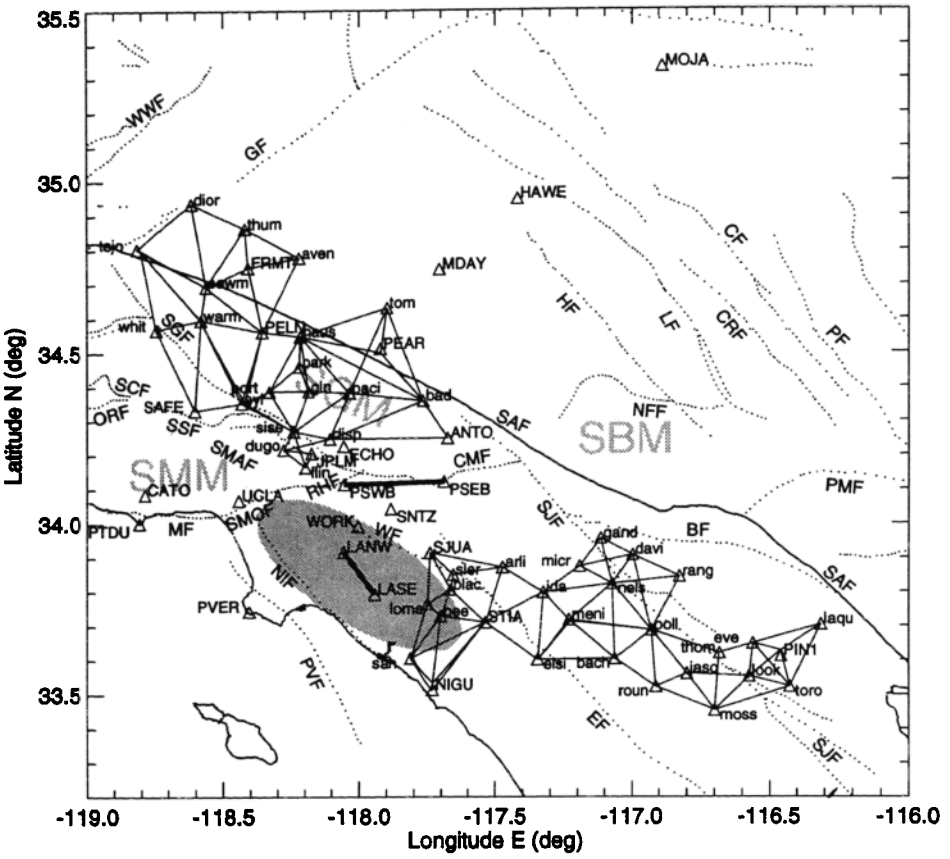

Figure 1. Los Angeles basin (shaded region) and its vicinity and the geodetic network. Triangulation and GPS stations are identified by their four-letter IDs in uppercase. Trilateration sites are identified by four-letter abbreviations of their names in lowercase. All the stations are marked by open triangles, but not all the station names or IDs are shown. Each group of stations whose velocities are tied together has one representative name or ID plotted. The thin lines are the trilateration baselines. The two thick lines are the baselines measured by historical taped distance. The faults are abbreviated as follows: BF, Banning fault; CF, Calico fault; CMF, Cucamonga fault; CRF, Camp Rock fault; EF, Elsinore fault; GF, Garlock fault; HF, Helendale fault; LF, Lenwood fault; MF, Malibu fault; NFF, North Frontal fault; NIF, Newport-Inglewood fault; ORF, Oak Ridge fault; PF, Pisgah fault; PMF, Pinto Mountain fault; PVF, Palos Verdes fault; RHF, Raymond Hill fault; SAF, San Andreas fault; SCF, San Cayetano fault; SGF, San Gabriel fault; SJF, San Jacinto fault; SMAF, Sierra Madre fault; SMOF, Santa Monica fault; SSF, Santa Susana fault; WF, Whittier fault; and WWF, White Wolf fault. The mountains are abbreviated as follows: SBM: San Bernardino Mountains; SGM: San Gabriel Mountains; and SMM,Santa Monica Mountains.

tude.) North of the basin, many of the earthquakes have thrust mechanisms, often coupled with left-lateral displacements. Examples include the 1971 San Fernando M 6.6, the 1987 Whittier Narrows M 5.9, the 1991 Sierra Madre M 5.8, and the 1994 Northridge M 6.7 earthquakes [*Working Group on California Earthquake Probabilities* (*WGCEP*), 1995].

Early geodetic studies in the Los Angeles basin [*Cline et al.*, 1984] revealed about 10 mm/yr convergence across the basin from San Pedro to Mount Wilson, but data available at that time were not good enough to make the estimate very accurate. North of the basin, *Cheng et al.* [1987] investigated more than 10 years of trilateration measurements and estimated 6 mm/yr convergence normal to the SAF along the Sierra Madre-Cucamonga fault system. *Lisowski et al.* [1991] used updated trilateration data and found little convergence within the San Gabriel Mountains normal to the SAF. Along the southern frontal fault system, *Shen* [1991] revealed about 3 mm/yr convergence. Using a combination of very long baseline interferometry (VLBI) and GPS measurements, *Feigl et al.* [1993] reported 5.0 ± 1.2 mm/yr shortening from Palos Verdes to the Jet Propulsion Laboratory (JPL), the latter being located in the SW foothills of the San Gabriel Mountains. West of the basin, *Donnellan et al.* [1993] used GPS methods to determine 7-10 mm/yr N-S convergence across the Ventura basin. A recent study by *Snay et al.* [1996] found that the SAF is located near the center of a deformation band whose central line in the Big Bend region

is oriented about 7° clockwise relative to the surface trace of the SAF.

Geodetic Measurements

Triangulation, Taped Distances, and Astronomical Azimuths

Horizontal geodetic networks in the Los Angeles basin were developed over a few phases during the past century. A triangulation network was established along the California coast in the late nineteenth century. This first-order network covered most of the Los Angeles basin and its vicinity. Observations were made at stations Castro 1898 (CAT0), San Fernando 1898 (SAF0), San Pedro 1853 (SPE0), Wilson Peak 1890 (WILP), Los Angeles NW Base 1889 (LAN0), Los Angeles SE Base 1889 (LASE), San Juan 1886 (SJUA), Niguel 1884 (NIG0), and Santiago 1899 (STIA). This network, observed during 1898 and 1899 in its first epoch, was reoccupied completely during the 1920s and 1950s. A taped distance was first measured in 1899 along a 17-km baseline between stations LAN0 and LASE, with its relative accuracy reported as about 10^{-5} or about 180 mm uncertainty for the baseline [*Bowie*, 1972].

The nineteenth century network was augmented by a group of stations west of the basin during the 1920s, which include Michelson 1923 (MICH), Antonio 1923 (ANTO), Pasadena West Base 1922 (PSWB), and Pasadena East Base 1922 (PSEB). These stations were connected to the earlier network at LAN0, LASE, SJUA, and WILP. The 1920s network was installed to support A. A. Michelson's speed-of-light experiment carried out between station MICH located at the peak of Mount Wilson and station ANTO at the peak of Lookout Mountain south of Mount San Antonio. A 36-km-long baseline between stations PSWB and PSEB was determined by adjusting a collection of angle and distance measurements. These measurements include Invar-taped distances between PSEB and PSWB, passing through a cluster of intermediate stations, and directions observed among MICH, ANTO, PSWB, PSEB, Pasadena East Base 2 1922 (PSE2), Dimas 1922 (DIMA), and Joaquin 1922 (JOAQ) [*Michelson*, 1927]. Uncertainty of this baseline is believed to be about 44 mm [*Michelson*, 1927]. This means a relative accuracy of 10^{-6}, an order of magnitude better than the Los Angeles baseline measured during the 1890s. The "Michelson baseline" provides high-accuracy scale control for the early triangulation network.

Additional stations were established in the basin during the 1930s; among them are stations Echo Rock 1933 (ECHO), Workman Hill 1932 (WORK), and San Tuze 1937 (SNT0). Observations were made at station WORK relative to the 1890s and 1920s stations in 1933. The three 1930s stations were occupied along with other stations in the network during the 1950s and 1960s. Station locations are shown in Figure 1, and their occupation histories are listed in Table 1.

Raw triangulation measurements are directions with respect to a reference direction. For most of the triangulation data we use here, the reference directions were not oriented to stations included in our study. For the sake of convenience, we use azimuth differences as the data, with one reference station chosen from our network in each epoch. The typical uncertainty of a direction measurement is about 3.5 μrad [*Gergen*, 1975]. We propagate uncertainties of the original directions to derive the uncertainties of the direction differences, assuming that the errors of the original directions are uncorrelated.

An astronomical azimuth is a direction pointing from a base station to another, measured from north in the horizontal plane of the base station. In the Los Angeles basin network, the astronomical azimuths were measured in two time epochs. Measurements of the first epoch were made between stations LAN0 and LASE in 1890. Measurements of the second epoch were made in the early 1920s; at that time, almost all the existing stations in the network had their astronomical azimuths measured relative to their triangulation partners. Errors of these astronomical azimuths are about 1.5 s (7 μrad) [*Carter et al.*, 1978].

Trilateration

Since the early 1970s, the California Department of Mines and Geology (CDMG) and subsequently the U.S. Geological Survey (USGS) have surveyed baseline lengths using electro-optical distance measuring (EDM) instruments in southern California. These observations are 1 order of magnitude better than the triangulation measurements [*Savage and Prescott*, 1973]. Data of about 20 years from two of the networks are used in this study: one is the Tehachapi-San Gabriel network north of the Los Angeles basin covering the San Gabriel Mountains area, and the other is the Anza network south of the Los Angeles basin spanning a region from the Newport-Inglewood fault west to the Coachella valley section of the SAF east. Errors of the data were found normally distributed with a standard deviation $\sigma = (a^2 + b^2L^2)^{1/2}$, where L is the distance measured, a = 3 mm, and $b = 2 \times 10^{-7}$ [*Savage and Prescott*, 1973; *King et al.*, 1987]. Not all stations in the two networks are used in this study. The ones being used are shown in Figure 1 and listed in Table 2. Note that the trilateration sites occupied also by GPS are listed in Table 1 rather than in Table 2.

GPS Measurements

GPS surveys in the Los Angeles basin and its vicinity started in 1987 (the very first measurements were made in 1986, but very few sites were observed) and were carried out by researchers from several universities and crews from government agencies such as the National Geodetic Survey (NGS) and USGS. The early measurements were made in a campaign mode, with each station occupied 1-3 days each time and several

Table 1. GPS-Triangulation Station Occupation List

ID	Stamping or Location	Latitude°N	Longitude°E	1890s	1920s	1930s	1950s	1960s	1986	1987	1988	1989	1990	1991	1992	1993
ANTO[a]	Antonio 1923	34.2485	-117.6751		A,T		T						G			G
CAT0[b]	Castro 1898	34.0857	-118.7857	T	T		T						G			
CAT3[b]	Castro 1898 Rm 3	34.0858	-118.7859				T									
CATO[b]	Solstice Cyn B2 Aux 1	34.0858	-118.7858							G		G	G		G	G
DIMA[c]	Dimas 1922	34.1139	-117.8185		A,T											
DS10[d]	TurboRogue Phase Center, Mojave	35.4252	-116.8893										G	G	G	G
ECH2[d]	Echo Rock 1933 Rm 2	34.2248	-118.0550										G			
ECHO[d]	Echo Rock 1933	34.2249	-118.0550				T	T		G			G	G	G	G
FRMT	Fremont Peak	34.7491	-118.4074												G	
HAWE	Hawes 1958 Rm 2	34.9481	-117.4184								G		G		G	
JOAQ[c]	Joaquin 1922	34.1140	-118.0385		A,T											
JPLM[f]	JPL Mesa, PGGA	34.2048	-118.1732										G	G	G	G
JPLA[f]	JPL Aries 1 1975	34.2047	-118.1710							G	G	G	G			G
JPLR[f]	JPL Aries 1 1975 Rm 1	34.2047	-118.1709										G	G		
LAN0[g]	LA NW Base 1889	33.9181	-118.0572	A,D,T	A,T		T									
LAN2[g]	LA NW Base 2 1956	33.9183	-118.0567				T	T								
LANW[g]	LA NW Base Aux 3 1963	33.9167	-118.0552					T							G	G
LASE	LA SE Base 1889 1957	33.7928	-117.9423	A,D,T	A,T	T						G			G	G
MDAY	Monday 1929	34.7430	-117.7059								G	G	G	G	G	
MIC1[d]	Michelson 1923 Rm 1	34.2225	-118.0578												G	
MICH[d]	Michelson 1923	34.2226	-118.0578		A,T											
MOJM[e]	MiniMac phase center, Mojave	35.3315	-116.8882									G	G	G		
MOJA[e]	TI4100 phase center, Mojave	35.3316	-116.8882							G	G					
MOJF[e]	FRPA-1 phase center, Mojave	35.3316	-116.8882									G				
NIG0[h]	Niguel 1884	33.5125	-117.7342	T	A,T	T	T	T								
NIGU[h]	Niguel A 1884 1981	33.5145	-117.7303						G			G		G		G
PEAR[i]	Pearblossom NCMN 1983	34.5121	-117.9224							G	G		G	G	G	G
PELN	Pelona 1932	34.5610	-118.3561												G	
PICO[j]	Pico NCER 1977	34.3306	-118.6013									G				G
PIN1[k]	Pinyon 1 PGGA	33.6122	-116.4582										G	G	G	G
PINY[k]	Pinyon Flat NCMN 1981	33.6093	-116.4588						G	G	G					
PSE2	Pasadena E Base 2 1922	34.1206	-117.6888		A,T		T	T								
PSEB	Pasadena East Base 1922	34.1213	-117.6885		A,D,T								G	G	G	
PSWB[c]	Pasadena West Base 1922	34.1139	-118.0533		A,D,T								G	G		G
PTDU	Point Dume Reset 1947	34.0016	-118.8067							G					G	
PVER[l]	Palos Verdes Aries 1976 1980	33.7438	-118.4036						G	G	G	G	G	G	G	

Table 1. (continued)

ID	Stamping or Location	Latitude°N	Longitude°E	1890s	1920s	1930s	1950s	1960s	1986	1987	1988	1989	1990	1991	1992	1993
SAF0[j]	San Fernando 1898	34.3298	-118.6010	T	T		T									
SAF3[j]	San Fernando 1898 Rm 3	34.3300	-118.6010										G			
SAFE[j]	San Fernando Aux2 Ecc1 Rm2 1967	34.3304	-118.6013							G		G	G			G
SJUA	San Juan 1886	33.9138	-117.7381	T	A,T	T	T	T		G				G		G
SNT0[m]	Covina C7 San Tuze 1957 1990	34.0425	-117.8835				T	T						G	G	
SNTZ[m]	Covina C7 Rm 1 1937	34.0425	-117.8837							G		G		G	G	G
SPE0[l]	San Pedro 1853	33.7461	-118.3360	T	A,T	T	T									
SPED[l]	San Pedro 1853 Rm 2	33.7463	-118.3364									G			G	
STIA[n]	Santiago 1899	33.7106	-117.5342	T	A,T	T	T	T			G					G
UCL0[o]	UCLA Slichter Hall Roof	34.0690	-118.4409								G				G	
UCLA[o]	Phase Center, UCLA Young Hall	34.0687	-118.4410										G	G	G	G
WD11[g]	Whittier D11 Reset 1976	33.9147	-118.0719		A,T							G		G		
WILP[d]	Wilson Peak 1890	34.2238	-118.0617	T	T		T									
WORK	Workman Hill 1932	33.9917	-118.0029			T	T	T				G		G		G

Superscript letters are group indices of velocity ties. A, astronomical azimuth; D, taped distance; T, direction; G, GPS.

stations observed simultaneously. All the stations are shown in Figure 1. All the measurements used in this study are listed in Table 1, which can be classified into three groups:

GPS-triangulation. The early GPS survey in the Los Angeles basin was designed partly to reoccupy the historical triangulation sites and their surrogates. The first GPS occupations of the sites are the following; 1986: Niguel A 1981 (NIGU, surrogate for NIG0); 1987: Solstice Cyn B2 Aux 1 (CATO, surrogate for CAT0), ECHO (surrogate for WILP), San Fernando Aux 2 Ecc 1 Rm 2 (SAFE, surrogate for SAF0), SJUA, Covina C7 Rm 1 1937 (SNTZ, surrogate for SNT0), and WORK; 1988: STIA; 1989: LASE, San Pedro Hill 1853 Rm 2 (SPED, surrogate for SPE0), and Whittier D11 1976 (WD11, surrogate for LAN0); 1990: ANTO, MICH, PSEB and PSWB. The local fiducial stations measured simultaneously during this time period were at Palos Verdes (PVER), JPL (JPLA and JPLM), and Pinyon Flat (PINY and PIN1). Because of urban development in the Los Angeles basin area, most of the historical sites are either destroyed or disturbed, requiring that some local stations with ties to the historical triangulation sites be used as surrogates. We give detailed description of those sites and the relationships between the original and the substitute sites in the appendix.

GPS-GPS. In this study we include also a group of sites that were designed to measure deformation using repeated GPS measurements solely. These occupations started in the late 1980s and their first GPS epochs are: 1987: Pearblossom NCMN 1983 (PEAR) and Pt. Dume 1947 (PTDU); 1988: Hawes 1958 Rm 2 (HAWE), Monday 1929 (MDAY), and UCL0. Those experiments were part of an orchestrated effort to study tectonic deformation in southern California by researchers from four universities: Massachusetts Institute of Technology, California Institute of Technology, U.C. Los Angeles, and U.C. San Diego [*Feigl et al.*, 1993]. More data were collected at those sites from 1990 to 1993 by UCLA crews. A number of the sites we use here including LANW, NIGU, PEAR, PICO, SAFE, SJUA, and WORK were also occupied by crews from several counties in southern California in 1993.

GPS-trilateration. In late 1992 the NGS and the Southern California Earthquake Center jointly conducted a GPS survey in the central Transverse Ranges area. Among the stations surveyed were USGS trilateration sites whose trilateration data are also used here. Trilateration surveys are designed for horizontal control purposes and lack the capacity to measure vertical deformation. Unfortunately, large errors in elevation can introduce significant errors to the horizontal control adjustment. GPS surveys, on the other hand, produce Three-dimensional (3-D) measurements which not only add new measurements but also effectively determine the station elevations and improve the quality of the horizontal control adjustment of the trilateration network.

Table 2. Trilateration Station List

ID	Latitude °N	Longitude °E
7-8-28[h]	33.5337	-117.7302
arling[p]	33.8711	-117.4714
arling80[p]	33.8710	-117.4715
asbesrm1[k]	33.6277	-116.4591
asbestos[k]	33.6276	-116.4592
bachelor	33.6054	-117.0623
bee	33.7290	-117.6996
black	33.8063	-117.6628
david	33.9082	-116.9968
elsinore[q]	33.6024	-117.3433
elsinrm4[q]	33.6024	-117.3433
eve[r]	33.6488	-116.5604
eve rm1[r]	33.6488	-116.5604
gander	33.9561	-117.1143
ida	33.7984	-117.3231
jason	33.5615	-116.7992
lomaaux2[s]	33.7652	-117.7464
lomancer[s]	33.7652	-117.7464
lomas[s]	33.7652	-117.7466
lookout	33.5533	-116.5741
menifee[t]	33.7182	-117.2288
micro[u]	33.8743	-117.1912
microrm1[u]	33.8742	-117.1911
moore[t]	33.7140	-117.2237
moss	33.4547	-116.6992
nelson	33.8230	-117.0707
niguel[h]	33.5125	-117.7342
pollycgs[v]	33.6879	-116.9265
pollydmg[v]	33.6878	-116.9265
ranger	33.8444	-116.8254
roundtop	33.5242	-116.9106
san[n]	33.7116	-117.5333
san 2[n]	33.7119	-117.5332
san joaq	33.6060	-117.8120
sier	33.8502	-117.6537
thom cgs[w]	33.6213	-116.6828
thom2asu[w]	33.6206	-116.6807
thomas[w]	33.6208	-116.6807
thomecc2[w]	33.6207	-116.6808
toro[x]	33.5236	-116.4258
toro 80[x]	33.5236	-116.4258
laquinta	33.7040	-116.3127
ant aux[a]	34.2487	-117.6751
avenue	34.7768	-118.2201
bad pow[y]	34.3584	-117.7646
camp 9[z]	34.3532	-118.4180
diorite	34.9345	-118.6152
dispoint	34.2466	-118.1051
dugo	34.2154	-118.2767
flint	34.1636	-118.1967
gln ncer[aa]	34.3869	-118.1848
hau ecc1[bb]	34.5476	-118.2155
hauser[bb]	34.5477	-118.2155
jpl1 rm1[f]	34.2048	-118.1708
littejon[cc]	34.8005	-118.8027
may[z]	34.3522	-118.4296
mtgleasn[aa]	34.3869	-118.1847
nbaldaux[y]	34.3587	-117.7646
pac1ncer[dd]	34.3829	-118.0340
pac2ncer[dd]	34.3818	-118.0346
pacifico[dd]	34.3819	-118.0346
park rm3[ee]	34.4597	-118.2188
parkaux2[ee]	34.4598	-118.2187
port[ff]	34.3863	-118.3298
port rm1[ff]	34.3866	-118.3298
saw ecc[gg]	34.6931	-118.5615
sawmill[gg]	34.6931	-118.5614
siselsie	34.2690	-118.2390
syl[z]	34.3522	-118.4296
tank[i]	34.5002	-117.9224
tejon 41[cc]	34.8036	-118.8156
thumb	34.8627	-118.4191
tom	34.6312	-117.8986
warm rm2[hh]	34.5953	-118.5800
warm spr[hh]	34.5955	-118.5798
whitaker	34.5675	-118.7428

Superscript lowercase letters are group indices of velocity ties.

Dozens more GPS stations have been observed in the Los Angeles basin area since 1991, at the frequency of one occupation or so each year. However, perturbations from the 1992 Landers and the 1994 Northridge earthquakes make it difficult to determine accurately the interseismic station velocities, because the data include also coseismic displacement signals caused by the two quakes. For the sites being studied here, measurements made after 1993 are excluded and coseismic displacements caused by the 1992 Landers quake are modeled.

GPS Data Processing

Observational sessions of the GPS measurements used for this study range from 6 to 24 hours long each day. Instruments used for data collection were TI4100 receivers before 1990 and mainly Trimble 4000SSTs after. Data are processed using GAMIT software [*King and Bock*, 1995] to produce daily or multiday solutions. Data collected from the GPS global tracking sites (CIGNET stations before 1990 and IGS after) are also used to solve for precise satellite orbits. In each solution, dual-frequency beat-phase data are used to compute double-difference ionosphere-free residuals, which are then inverted through a least squares procedure solving for the unknown parameters. These include station positions, satellite orbital elements, phase ambiguity integer numbers, tropospheric delay residuals, etc. Uncertainty of 10 mm is assumed for the carrier beat phase data. For a detailed description of the data processing method, please refer to *Dong and Bock* [1989], *King and Bock* [1995], and *Feigl et al.* [1993].

Data Corrections

Corrections are needed for the triangulation measurements to compare them with predictions from a known Earth model. One correction is for deflection of the local vertical. We neglect this correction because preliminary calculations show that the largest error caused by neglecting it in our network would be about 0.35 s (1.7 μrad) at stations PSEB and ANTO. This is much smaller than our data errors. See the ap-

pendix of *Sauber et al.* [1989] for an example of analysis with and without corrections for deflection of the vertical; the corrections are negligible. Another correction to the triangulation measurements is the skew normal correction, which should not exceed 0.1 s (0.48 μrad) because the maximum elevation difference between observational stations is no more than 1 km [*Bomford*, 1980]. We ignore this correction too.

A taped distance is measured from mark to mark. A correction has to be applied to convert the mark-to-mark distance into a geodesic on the surface of an ellipsoid, which is the WGS84 ellipsoid here to fit into our model. Such corrections are made following *Vincenty* [1975].

A Laplace correction is required for the astronomical azimuths in order to convert them into a geodetic coordinate system. This process corrects the bias caused by the coordinate difference between the Clarke 1866 coordinate used for historical triangulation and the WGS84 coordinate used for GPS. Such correction is made according to *Bomford* [1980].

Systematic scale difference may exist between GPS and EDM measurements. *Svarc et al.* [1994] found such a difference of 0.300 ± 0.067 ppm for EDM-GPS. In our later modeling work we try both with and without application of such a correction to the EDM line length data. Because the ties between the two data set are mainly from the velocity constraints rather than from the station position constraints, we find that introduction of the correction has virtually no effect on the final results.

Station Velocity Adjustment

From the above descriptions, we have a composite data set which includes 343 triangulation angles, 1345 EDM line lengths, 17 azimuths (including two local tie measurements), 12 taped distances (including 10 local tie measurements), and 119 GPS solution files containing from one to 33 baseline vectors. When made within a global fiducial network, GPS measurements can determine 3-D station positions in a global coordinate frame. By comparison, triangulation measurements can determine shear strain changes within a network but cannot determine the network's size and orientation changes. Such deficiencies can be remedied by adjusting a data set which combines together triangulation, taped distance, and astronomical azimuth measurements. If we assume a constant strain rate for the last century except for episodic changes due to large earthquakes, using the early triangulation, taped distance, and azimuth data along with the recent GPS measurements, we can determine the deformation rates including the dilatation and rotation rates in our Los Angeles basin network up to 10^{-8} accuracy. The USGS trilateration networks have about 20 years of occupation history and offer more detailed local resolution. The trilateration data can resolve the strain and size changes but not the orientation change of the network, and they cannot by themselves tie coordinates to a global reference frame. Error accumulation usually has a higher rate from one side of the network to the other, compared to GPS. In this study the GPS and the trilateration networks share some common stations or have stations close to each other geographically, so that their velocities can be tied together. In doing so, we effectively eliminate the orientation deficiency of the trilateration network, greatly reduce the velocity errors of the marginal trilateration sites, and tie all the networks into one geodetic frame. All the velocity ties are listed in Tables 1 and 2. There are two kinds of ties: one is for the stations close to each other and believed to be located in the same tectonic domain; the other is for those measured at one time epoch only whose ties to other nearby stations help stabilize the solution.

We model the station displacements with constant interseismic velocities plus episodic coseismic displacements at times of significant earthquakes. Studies of 20 years EDM observations showed no significant temporal variations except at a few locations [*Savage and Lisowski*, 1995a, b], suggesting that the constant interseismic velocity assumption is valid for combining 20 years trilateration with 6 years GPS. However, such studies would not automatically justify combination of century old triangulation with the GPS and EDM data. The most significant time dependent signals for interseismic deformation are usually from postseismic deformation following large earthquakes, which can cause significant acceleration of surface deformation in the epicentral region. The only quake which might have caused significant postseismic displacements to the triangulation sites in the Los Angeles basin area is the 1857 M 8.3 quake which ruptured the SAF from San Bernardino to the Carrizo plain [*Thatcher*, 1983]. However, 40 years had passed since the quake when the first triangulation measurement was made in the basin. The postseismic deformation would have died out substantially, and its remaining effects would probably be negligible comparing to the constant deformation rates at the sites. Therefore the constant deformation rate assumption may also hold for triangulation data used in this study.

In the time span of our data coverage, four earthquakes occurred in the network and measurably disturbed at least one station in the network. They are the 1971 M 6.6 San Fernando earthquake, about 22 km ENE of station SAFE; the 1989 M 5.9 Whittier Narrows earthquake, right beneath station WORK; the 1991 M 5.8 Sierra Madre earthquake, which caused possible centimeter level displacements at stations ECHO, JPLM, and PSWB; and the 1992 M 7.3 Landers earthquake, which affected all stations in southern California. We need to model the coseismic displacements at the sites but not the postseismic displacements, because the postseismic effects are indistinguishable from the coseismic effects in our data which were collected either long after the quake or only one epoch was measured since (i.e., the Landers quake).

The velocity adjustment algorithm is

$$O_j(t) - O_j[\vec{X}_i(t_0)] = \sum_i (\nabla_i O_j)\cdot\vec{D}_i$$

$$+(t-t_0)\sum_i (\nabla_i O_j)\cdot\vec{V}_i - \sum_k H(T_k-t)\sum_i (\nabla_i O_j)\cdot\vec{E}_{ik}+\epsilon_j$$

where $O_j(t)$ is the jth observable, which can be an angle, a distance, an azimuth, or a component of a GPS baseline vector; t_0 is a reference time epoch; $\vec{X}_i(t_0)$ is the initial position of the ith station at time t_0; $O_j[\vec{X}_i(t_0)]$ is the corresponding value predicted from initial station positions; $\vec{D}_i$ is unknown, the ith station initial position correction; $\vec{V}_i$ is unknown, the ith station velocity; $\vec{E}_{ik}$ is unknown, the coseismic displacement of kth earthquake at ith station; T_k is the kth earthquake epoch; $H(T_k - t)$ is the Heaviside stepfunction; and ϵ_j is the random error for the jth measurement.

Triangulation and trilateration data lack good control for vertical components. GPS data can resolve vertical positions but with uncertainties of a few centimeters [*Larson and Agnew*, 1991], too large to resolve the interseismic displacements. Such displacements were probably no more than a centimeter during the entire period the data were collected. Therefore our velocity adjustment is performed in Two-dimensional space. In the modeling algorithm described above, each datum is converted to the equivalent geodesic, angle, or azimuth observable on the surface of a WGS84 ellipsoid and is compared with that predicted by a model. To solve for the unknowns, the data residuals are then inverted using least squares along with a priori constraints such as the station velocity ties. The treatment of the a priori information follows *Jackson* [1979] and *Jackson and Matsu'ura* [1985].

We also use VLBI data to constrain station velocities at several fiducial sites located at JPL, Goldstone, Pearblossom, Pinyon Flat, and Palos Verdes. The VLBI velocities are taken from Table 4.2 of *Ma et al.* [1994], and are rotated from the NUVEL-1 NNR model frame to the North-American-plate-fixed coordinate frame. The rotation parameters are obtained from *Argus and Gordon* [1991]. We then convert all velocities relative to station Goldstone, and use them and their uncertainties as the a priori data for our velocity adjustment. All intercorrelations between the VLBI velocity vectors are ignored. Errors caused by such negligence are minimal when station Goldstone is selected as the reference site because the velocity uncertainties for this site (2 mm/yr) are significantly smaller than those for all other VLBI sites (5-11 mm/yr) used here.

In the inversion the GPS baseline vector data are weighted by the inverse of their covariance matrix to properly account for the correlation between different baselines and between the baseline components. We also attempt to balance weights between different data types. We assign a scaling coefficient for each data group and examine the postfit residuals of each group to estimate their proper weight, i.e., whether the normalized postfit χ^2 per degree of freedom of each group is close to one. If not, we reassign the scaling coefficients and redo the inversion. Our best fit solution gives the coefficients for the angle, azimuth, taped distance, EDM line length, and GPS data as 1.0, 1.0, 1.0, 1.5, and 3.5, indicating that the uncertainties of only the GPS and EDM measurements need to be adjusted substantially.

Examples of input data and their fits to the model are shown in Figure 2: Figures 2a and 2b are the angle and line length measurements, respectively, and Figures 2c and 2d are the east and north components of the GPS baselines, respectively. Each GPS site was usually observed many more times than the number of data points shown for two reasons. One is that the two stations in a pair were not always observed simultaneously. Another reason is that a single data point sometimes represents a multiday solution of 2-3 consecutive days measurements, which is usually true for the early year results from 1986 to 1988 (to better resolve the satellite orbits).

Station Velocity Results and Analysis

Results

Our resolved station velocities are shown in Figure 3 and listed in Table 3; x denotes the east component and y denotes the north component. The postfit χ^2 per degree of freedom of the observation data is around 1.0, indicating a reasonable fit to the data. Stations ECH0 and PVER are chosen as reference and held fixed in Figures 3a and 3b, respectively. Only one representative is plotted if velocities of several stations are tied together; for example, LANW also represents LAN0, LAN2, LAN3, and WD11. The result shows that the sites located NW of the network have larger uncertainties than the other sites in the network, because the trilateration sites there lack good control over rotation at the network edge there.

We notice from Figure 3 (also from later residual studies) that the velocity field seems quite smooth across the network except in the Los Angles basin, where a few sites such as WORK, LANW, LASE, and SJUA show a bit more local scatter. This reflects the difficulty of obtaining good measurements in the basin, where most of the sites are in sediments and suffer from various problems. Station WORK has been reset three times including twice during our GPS survey time period, and we had to toss out early measurements. The original triangulation site at Los Angeles NW Base (LAN0) was destroyed, and there is no good tie to link the triangulation site to the GPS site LANW. Station LASE was reset during the time period between the last triangulation survey and the first GPS survey, and the sky at the site is partially obstructed for GPS observation. Nevertheless, these complications are limited to a local region and some useful conclusions can still be drawn.

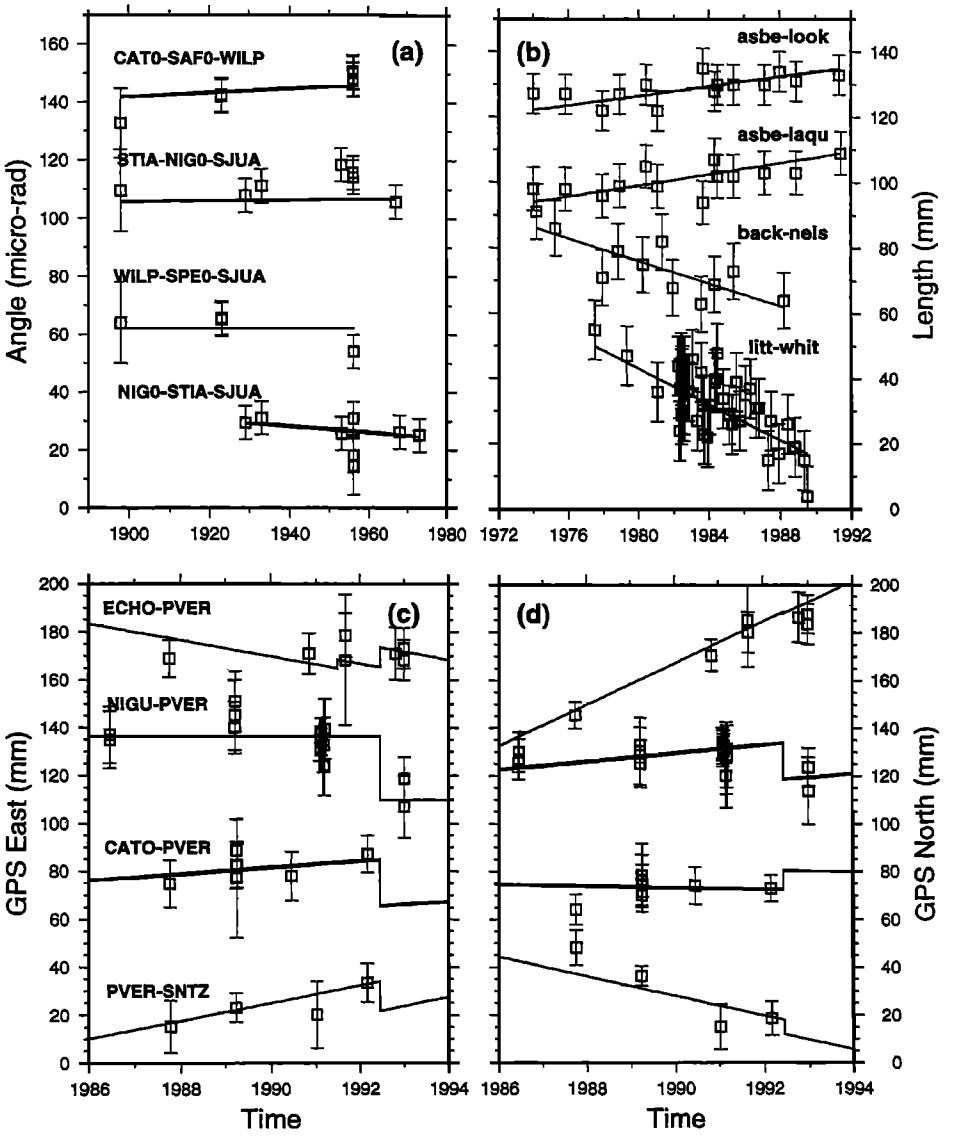

Figure 2. Examples of geodetic measurements. (a) triangulation angles, (b) EDM line lengths, (c) GPS east components, and (d) GPS north components. The error bars represent the standard deviations used in the data adjustment; i.e., 1.0, 1.5, and 3.5 formal standard deviations for the triangulation, EDM, and GPS data, respectively. The solid lines are predictions from the adjustment. The kinks on the lines are the predicted coseismic jumps of the earthquakes.

A number of features can be seen from the velocity field:

1. South of 33.9°N latitude, crustal deformation is dominated by displacements parallel to the major strike-slip faults: the SAF, the SJF, the Elsinore fault, and the Newport-Inglewood fault. This observation is consistent with the finding of *Lisowski et al.* [1991]. The strike-slip rate difference across the SJF is about 10 ± 2 mm/yr, 4 ± 2 mm/yr across the Elsinore fault, and 3 ± 2 mm/yr across the southern portion of the Newport-Inglewood fault and the Palos Verdes fault.

2. N-S convergence is found in the northern part of the Los Angeles basin, along the Malibu-Santa Monica-Raymond Hill fault zone, and along the Santa Susana-Sierra Madre-Cucamonga fault zone. The baseline length shortening rates are about 2 ± 1 mm/yr between CATO and SAFE, 2 ± 1 mm/yr between UCLA and SAFE, 4 ± 1 mm/yr between PSWB and ECHO, and 4 ± 1 mm/yr between PSEB and ANTO. Convergence from PVER to ECHO is about 6 ± 1 mm/yr, consistent with the finding of *Feigl et al.* [1993].

3. Along the Mojave section of the SAF, the SAF seems to govern the deformation in the region. This finding is again consistent with the result of *Lisowski et al.* [1991].

4. In the Mojave desert, dominant features are screw dislocation motion from the SAF and strike-slip motion across the Mojave Shear Zone, which is the southern part of the Eastern California Shear Zone. Such a strike-slip motion across the Mojave Shear Zone is about 5 ± 3 mm/yr from HAWE to MOJA in our solution. This is close to the finding of *Savage et al.*'s [1990]

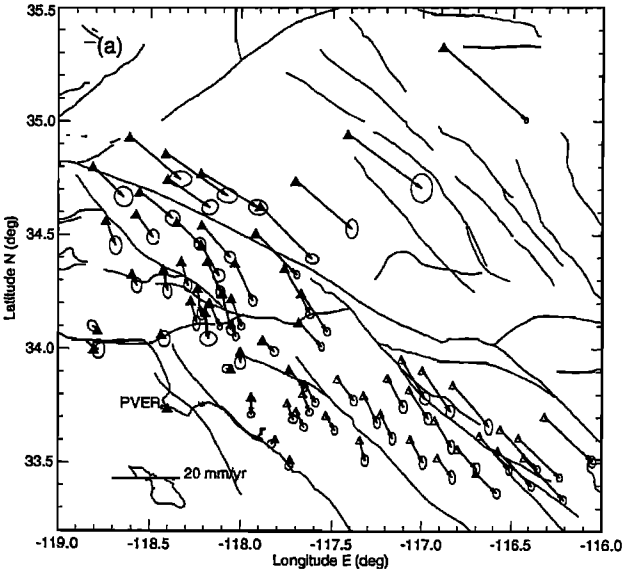

Figure 3a. Interseismic velocity solutions with respect to station PVER. Solid triangles denote the sites shown in a velocity profile across the Mojave section of the SAF. The error ellipses are one standard deviation.

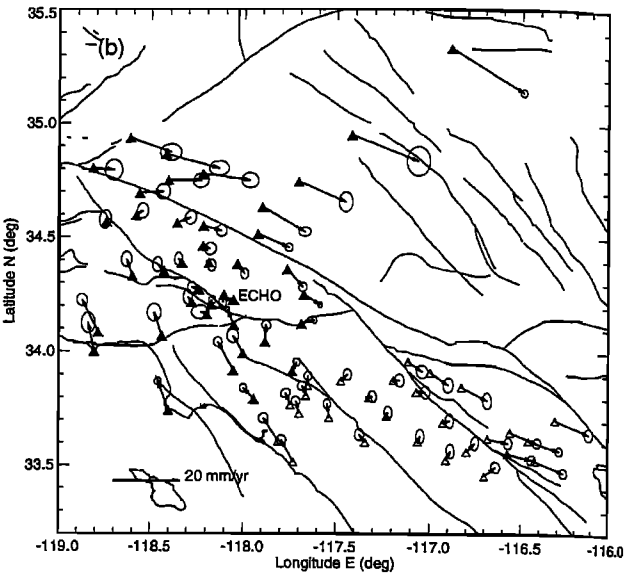

Figure 3b. The same as Figure 3a, except that the velocity solutions are with respect to station ECHO.

Table 3. Station Velocities

Stations	V_x^o, mm/yr	V_x^p, mm/yr	$V_x^o - V_x^p$, mm/yr	σ_x, mm/yr	V_y^o, mm/yr	V_y^p, mm/yr	$V_y^o - V_y^p$, mm/yr	σ_y, mm/yr	C_{xy}
ANTO	8.0	8.6	-0.6	1.0	-11.3	-6.4	-4.9	1.2	-0.18
CATO	-1.5	1.2	-2.8	1.4	0.9	-0.1	1.0	1.6	-0.19
ECHO	3.2	4.8	-1.7	1.0	-8.3	-3.9	-4.5	1.0	0.11
FRMT	13.0	13.3	-0.4	2.4	-8.4	-7.8	-0.7	2.1	0.13
HAWE	22.6	22.9	-0.3	3.2	-15.9	-16.6	0.7	4.2	0.00
JPL1	3.2	4.0	-0.7	0.7	-7.0	-3.1	-3.9	1.0	0.01
LASE	0.0	0.9	-0.9	1.0	-5.3	-1.2	-4.1	0.9	0.08
LANW	-0.3	1.5	-1.8	1.2	-0.2	-1.4	1.2	1.2	0.01
MDAY	17.1	19.8	-2.7	1.8	-14.2	-13.8	-0.4	2.8	0.00
MOJA	25.4	25.6	-0.3	0.6	-21.6	-18.5	-3.1	0.8	0.02
NIGU	-0.3	0.4	-0.7	1.1	-1.8	-0.3	-1.5	1.2	0.00
PEAR	12.3	11.8	0.4	0.8	-12.3	-8.3	-4.0	1.1	-0.03
PELN	7.2	7.9	-0.7	1.7	-6.7	-5.1	-1.7	1.9	-0.02
PIN1	12.6	10.6	1.9	0.8	-11.8	-6.1	-5.7	1.1	0.03
PSEB	7.1	5.8	1.3	0.9	-7.3	-4.8	-2.6	1.2	-0.06
PSWB	1.4	3.4	-2.0	1.0	-3.9	-2.6	-1.3	1.2	-0.01
PTDU	1.4	0.7	0.7	1.9	-0.2	0.2	-0.3	2.8	0.00
SAFE	1.5	2.8	-1.3	1.5	-3.5	-2.3	-1.2	2.2	-0.04
SJUA	4.6	2.6	2.1	0.9	-5.7	-2.4	-3.3	0.9	0.01
SNTZ	3.6	3.3	0.3	1.2	-3.5	-2.8	-0.7	1.3	-0.04
STIA	2.6	1.8	0.8	0.9	-4.4	-1.6	-2.8	1.3	0.01
UCLA	1.0	1.9	-0.9	1.8	-1.6	-1.0	-0.6	2.3	0.00
WORK	0.1	2.3	-2.2	1.6	-3.4	-1.9	-1.4	1.9	0.00
arling	5.1	3.7	1.4	1.1	-6.5	-3.2	-3.3	1.5	-0.01
bachelor	3.9	3.9	-0.0	1.0	-6.9	-2.7	-4.1	1.9	0.09
bee	2.3	1.3	1.0	1.1	-4.7	-1.3	-3.4	1.1	0.02
black	2.1	2.0	0.0	1.1	-5.5	-2.0	-3.5	1.1	0.09
david	8.7	8.7	-0.1	1.3	-12.1	-7.6	-4.5	1.9	0.12
elsinore	1.6	2.1	-0.5	1.0	-6.1	-1.4	-4.6	1.6	0.06
eve	11.5	10.0	1.5	0.9	-11.8	-6.1	-5.7	1.2	0.01
gander	7.3	8.3	-1.0	1.5	-11.4	-7.2	-4.2	1.8	0.00
ida	4.2	3.7	0.5	1.0	-8.1	-3.1	-4.9	1.6	-0.02
jason	5.7	5.9	-0.2	1.0	-5.9	-3.5	-2.5	1.9	0.14
lomas	1.8	1.3	0.5	1.2	-4.9	-1.4	-3.4	1.1	0.11
lookout	10.5	8.5	1.9	0.9	-10.4	-4.7	-5.7	1.2	0.02

Table 3. (continued)

Stations	V_x^o, mm/yr	V_x^p, mm/yr	$V_x^o - V_x^p$, mm/yr	σ_x, mm/yr	V_y^o, mm/yr	V_y^p, mm/yr	$V_y^o - V_y^p$, mm/yr	σ_y, mm/yr	C_{xy}
menifee	3.7	3.7	0.0	1.0	-7.4	-3.0	-4.4	1.8	0.08
micro	4.9	5.7	-0.8	1.2	-8.5	-5.0	-3.5	1.8	0.00
moss	6.6	5.8	0.8	1.1	-5.9	-2.6	-3.3	1.4	0.00
nelson	5.9	6.2	-0.3	1.1	-8.5	-5.4	-3.1	1.8	0.01
pollycgs	5.2	6.1	-0.9	1.0	-7.8	-4.6	-3.2	2.0	0.02
ranger	11.0	9.7	1.3	1.2	-12.3	-7.8	-4.5	2.3	0.00
roundtop	4.5	4.4	0.1	1.0	-5.8	-2.5	-3.3	2.0	-0.17
san	0.0	-1.1	0.5	-0.8	-1.5	-1.5	-0.7	1.2	0.10
sier	3.4	2.5	0.9	1.0	-5.6	-2.3	-3.2	1.2	0.07
thomas	9.3	8.3	1.0	0.9	-10.0	-5.2	-4.8	1.5	0.01
toro	12.0	9.8	2.2	1.0	-12.4	-5.1	-7.3	1.2	0.00
laquinta	14.3	14.0	0.3	1.2	-13.0	-8.9	-4.1	1.7	0.00
avenue	17.0	16.3	0.8	2.7	-10.2	-9.8	-0.5	2.2	-0.10
bad	0.0	7.7	10.4	-5.9	-2.7	-13.5	-7.7	1.3	1.40
diorite	15.3	17.2	-1.9	3.4	-12.5	-9.7	-2.9	2.3	-0.01
dispoint	2.7	4.7	-2.0	1.2	-10.7	-3.8	-6.9	1.6	-0.01
dugo	1.9	3.5	-1.5	1.1	-6.8	-2.7	-4.1	2.2	-0.01
flint	1.1	3.4	-2.3	2.5	-7.9	-2.5	-5.4	2.0	0.00
gln	0.0	4.0	5.9	-4.5	-1.9	-9.2	-4.7	1.3	1.70
hauser	8.5	9.1	-0.7	1.6	-9.7	-6.0	-3.7	1.7	-0.12
pacifico	5.4	7.0	-1.7	1.2	-11.3	-5.5	-5.8	1.5	-0.11
park	0.0	5.3	6.8	-4.3	-1.4	-9.2	-4.9	1.8	1.80
port	2.1	4.8	-2.7	1.2	-7.2	-4.0	-3.2	1.8	-0.02
sawmill	10.1	9.8	0.3	2.2	-7.9	-5.7	-2.2	2.2	-0.06
siselsie	1.2	4.2	-3.0	1.2	-7.7	-3.5	-4.2	1.7	-0.09
syl	1.3	3.9	-2.6	1.3	-6.5	-3.4	-3.1	2.2	-0.11
tejon	41.0	9.3	10.9	-2.6	-1.6	-9.0	-6.4	2.7	2.90
thumb	18.8	16.7	2.1	3.0	-12.5	-9.5	-2.9	2.1	-0.08
tom	15.6	15.6	-0.0	1.9	-15.6	-10.6	-5.1	1.4	-0.10
warm	0.0	5.1	6.4	-2.9	-1.3	-7.0	-4.1	1.8	2.20
whitaker	3.0	4.3	-1.3	1.8	-7.6	-3.3	-4.3	2.7	-0.03
PVER	0.0	0.0	0.0	0.1	0.0	0.0	0.0	0.1	0.00

V^o, observed station velocity; V^p, model predicted station velocity; σ_x, σ_y, standard diviations of velocity components; and C_{xy}, correlation between velocity components x and y.

8 mm/yr but less than *Sauber et al.*'s [1994] 12 mm/yr across the Mojave Shear Zone.

Velocity Profile Across Mojave Section of SAF

Figure 4 shows the velocity components parallel and normal to the SAF for a station group (solid triangle sites in Figure 3) along a profile across the Mojave section of the SAF which strikes N65°W. Velocities of three island sites are also displayed to extend the profile farther SW; their values with respect to station PVER are obtained from *Feigl et al.* [1993]. We compare these data with predicted station velocities from a simple dislocation fault model with the SAF and the SJF included. In the model, the Earth is assumed to be an elastic half-space, and the faults are locked to 20 km depth. At depth, the SAF moves at a rate of 34 mm/yr through the Carrizo Plain section, 30 mm/yr along the Mojave section, 24 mm/yr along the San Bernardino Mtn section, and 25 mm/yr along the Coachella valley section. At depth, the Imperial fault is assumed to slip 34 mm/yr. The SJF moves underneath at a rate of 12 mm/yr. This model follows the fault slip estimates along the SAF and the SJF in a report by *WGCEP* [1995]. Although it is simple, this model has included all single fault segments whose slip rates are above 10 mm/yr and is believed to represent the major part of the crustal deformation field in southern California.

Although the fault-parallel motion of the stations demonstrates a sigmoidal pattern centered on the SAF, it is evident from Figure 4a that the model does not describe the parallel motion of the stations adequately. The observed strain rate spreads over an area broader than the model predicts, and the observed strain rate is significantly lower than the prediction close to the fault. As drawn, with the observed and predicted velocities measured with respect to a point on the SAF, the observed velocity between the SAF and the farthest point to the SW agrees well with the predicted value. Northeast of the SAF, however, the observed and predicted values diverge. At Mojave, the farthest site to the NE, the observed velocity is approximately 6 mm/yr greater in the SE direction than the model prediction. It appears that the major discrepancy occurs at just one site, MOJA. Because the relative velocity between

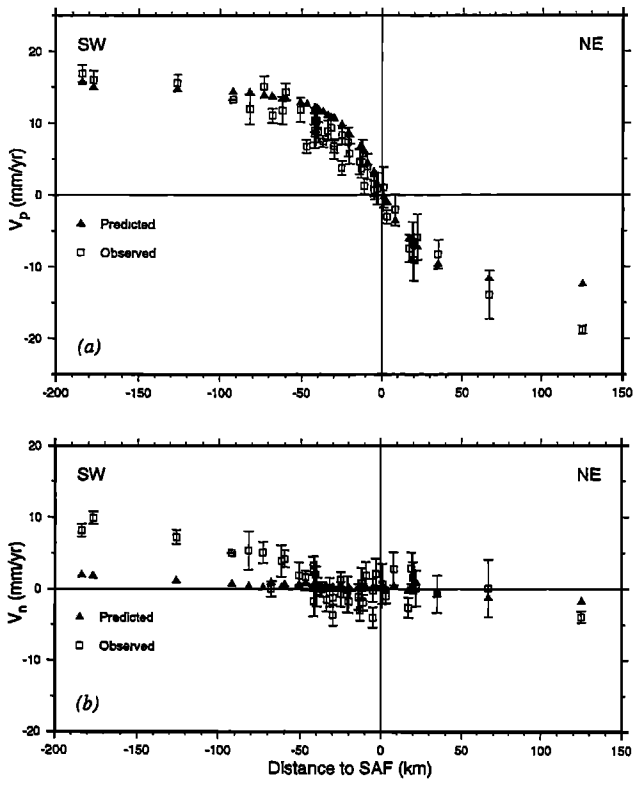

Figure 4. Station velocity profile (a) parallel and (b) normal to the Mojave section of the SAF. Stations shown here are denoted by solid triangles in Figure 3. Open squares are the velocity solution components with one standard deviation error bars, and solid triangles are the velocity components predicted from a fault model described in the text. The SAF is located at $x = 0$ and shown by a vertical line.

Mojave to the NE and Palos Verdes to the SW of the SAF is well constrained by VLBI measurements, the simplest explanation for this discrepancy is that one or more right lateral faults contribute at least 6 mm/yr in the eastern Mojave desert. However, the decision to refer displacements to a point on the SAF is completely arbitrary, and in principle, any constant may be added to the predicted curve. If this constant were chosen to minimize the sum of squared residuals, the discrepancy between the observed and predicted would be spread more evenly among the stations. Even so, the observed velocity gradient would still be much less than that observed near the SAF, and station MOJA would still stand out as anomalous.

The parallel motion discrepancy could be interpreted in different ways. One explanation is that the model does not include all faults which contribute to the region's crustal deformation. However, we know of no other major strike-slip faults that are sufficiently active to explain the discrepancy. Another possibility is that the simple model does not describe the SAF and the SJF properly. For example, the locking depths and slip rates given in the model may not be correct. Previous geodetic studies for this area tried tackling the problem [*Cheng et al.*, 1987; *Eberhart-Phillips et al.*, 1990; *Lisowski et al.*, 1991]; because of the limited areal coverage of the networks, these studies could not simultaneously resolve both the locking depth and the slip rate. Numerous geological studies have determined the average slip rate in the area [*Sieh et al.*, 1989; *Biasi and Weldon*, 1994; *Salyards et al.*, 1992], although the answers range from 20 to 36 mm/yr. A compromise estimate by *WGCEP* [1988, 1995] placed 30 mm/yr along this section of the SAF. *Sieh and Jahns* [1984] estimated 34 mm/yr relative motion along the SAF at Wallace Creek on the Carrizo plain. If we assume convergence is negligible on the Carrizo plain, the rate and the orientation of the SAF define the velocity of relative plate motion across the SAF in central California. If we also assume that the velocity in central California also represents the relative plate motion through the Mojave section of the SAF, the along-fault strike component would be about 31 mm/yr. If the convergence along the SAF in central California is not negligible and a 7° obliquity of relative plate motion with respect to the strike of the SAF is assumed there [*Humphreys and Weldon*, 1994], the along-fault strike component would be about 29 mm/yr. SW of the SAF, geological studies have shown that the San Gabriel fault is inactive [*Crowell*, 1973; *Ehlig et al.*, 1975; *Ehlig*, 1975], and there are no other strike-slip faults to diversify the NW trending shear motion from the Carrizo plain down to the San Gabriel Mountains. NW of the SAF, slip along the Garlock fault and White Wolf fault may diversify the NW trending shear motion somewhat and further reduce the tangential slip on the SAF. However, such reduction is probably minor because of the low slip rates along the two faults. Therefore we consider that the 30 mm/yr strike-slip motion is reasonable for the Mojave section of the SAF. Seismic studies revealed that the earthquake depths are relatively shallow, about 12-18 km along the Mojave segment of the SAF [*Webb and Kanamori*, 1985; *Jones*, 1988; *Hill et al.*, 1990]. If we use these estimates for the slip rate and the locking depth, the velocity discrepancy between the observed motion parallel to the SAF and the motion predicted by the model SW of the SAF would not be reduced. Other explanations must be found.

We propose that the broadening of the observed velocity profile shown in Figure 4a is caused by different scenarios: detachment motion in the lower crust or upper mantle, viscoelastic behavior of the Earth, a broad deformation across the SAF, or a combination of the three. Detachment motion has been proposed based on geological data [*Davis et al.*, 1989; *Shaw and Suppe*, 1996] in the Los Angeles basin area. Seismic studies revealed that the San Gabriel Mountains lack of a "root" sufficient to support the weight of the mountains, implying a possible horizontal detachment underneath [*Hadley and Kanamori*, 1977; *Hearn and Clayton*, 1986; *Sung and Jackson*, 1992]. Such a detachment would reduce the basal traction at the detachment

surface, thus weakening the lateral driving force transmitted from the lower to the upper crust and changing the loading mechanism from "vertical loading" toward "horizontal loading" [*Gilbert et al.*, 1994]. This would make the deformation pattern broader. Theoretical viscoelastic models and models based on realistic parameters of the SAF have been developed [*Nur and Mavko*, 1974; *Rundle and Jackson*, 1977a; *Savage and Prescott*, 1978; *Thatcher*, 1983; *Li and Rice*, 1987]. Such models usually assume an elastic plate overlying a viscoelastic half-space. Model predictions vary depending on the parameters used. However, two distinct features are usually shared by these models. One is that given the same locking depth, the deformation predicted by the viscoelastic models is broader at the Earth's surface than that predicted by elastic half-space models. Similar to the detachment case discussed above, this occurs because there is no strong basal traction transmitting lateral driving force from the viscoelastic lower plate to the elastic upper plate. Therefore the horizontal loading mechanism starts taking effect. The other feature is that the strain rate is time dependent, decreasing with time near the fault and increasing far away as coseismic stress is redistributed. Both features are consistent with our observations. Seismological studies suggested that decollement exists across the SAF [*Hadley and Kanamori*, 1977] and subduction might be taking place beneath the central Transverse Ranges [*Humphreys and Clayton*, 1990]. If these models are valid, the SAF would be offset at depth by decollement and subduction, causing a much broader deformation zone than predicted for a simple model with only a vertical SAF.

The observed normal components of the velocities (Figure 4b) close to the SAF are fairly consistent with that predicted by the WGCEP model, showing no compression in the San Gabriel Mountains within 40 km from the SAF. This part of the profile is similar to that in Figure 10 of *Lisowski et al.* [1991], as it should be since the trilateration data used in the two studies are about the same. About 40 km SW of the SAF, convergence normal to the fault occurs mostly along the south and SW frontal faults and within the Los Angeles basin and the San Fernando Valley. The rate is about 5 $\pm$ 1 mm/yr from PVER to PEAR. Farther from the SAF offshore, the rate seems to increase gradually, up to 8-10 mm/yr at BLUF and TWIN. This trend may reflect a gradual change in the relative motion direction from the local plate motion to the one between the Pacific plate and the North America plate, the latter being about 7° clockwise with respect to the former [*Humphreys and Weldon*, 1994; *Snay et al.*, 1996]. However, the three island velocities are obtained from another study [*Feigl et al.*, 1993] and integrated to this study with a common link at station PVER. Thus any errors for these three stations would be highly correlated, possibly causing an apparent velocity contrast between the islands and mainland. Caution should be taken when interpreting solutions at the three island sites.

WGCEP Model Comparison

The Southern California Earthquake Center recently released a report assessing the earthquake probabilities in southern California [*WGCEP*, 1995]. The report listed estimated fault slip rates for so called "type A" fault segments: those whose slip rates are believed greater than or equal to 3 mm/yr and whose earthquake histories for the last several events are known. The report listed also some fault zones labeled "type B" and "type C," whose earthquake histories are not well known. We adopt type A fault segments and some type B and C fault zones whose slip rates equal or exceed 3 mm/yr to make a forward model of the crustal deformation. The type A segment information is from Table 1 and the type B and C zone information is from Table 5 and Figure 3 of *WGCEP* [1995]. Ventura basin region is cut by several thrust faults but only an averaged fault slip rate is specified in *WGCEP* [1995] for the region. *Petersen et al.* [1996] offered a more detailed fault model for Ventura basin, whose total seismic moment there is consistent with that of *WGCEP* [1995]. Thus we adopt the fault slip rates of *Petersen et al.* [1996] for the Ventura basin faults. All the fault parameters are given in Table 4, except the fault widths below locking depths which will be discussed later in this section. For dislocation modeling, we specify additional model parameters undefined in the WGCEP report. For example, we assume that the SAF extends from NW and SE endpoints in the report to infinity, following its strike directions and slip rates there. The same is true for the Eastern California Shear Zone north extension. We assume uniform 20-km locking depths for all the faults. All the vertical strike-slip faults are assumed to have infinite fault width. The Palos Verdes fault is treated as dipping 45° SW [*WGCEP*, 1995] and extending to infinity below the locking depth. The Eastern California Shear Zone is modeled as a single fault. This representation differs from previous findings [e.g., *Sauber et al.*, 1994] that apportioned the Eastern California Shear Zone at the Mojave desert across several strands of faults. However, the difference should not significantly affect our modeling because our data coverage is sparse in the region and all the major faults north of the Mojave Shear Zone are located between stations HAWE and MOJA; our model reveals only the gross effect and not the details of the slip distribution along the faults. It is still an open question how thrust faults behave beneath seismogenic depths; we will model them under two possible scenarios to be discussed next.

We adopt the elastic half-space model and use dislocation theory to propagate fault slip into displacements at the earth's surface [*Okada*, 1985, 1992]. We consider such a model adequate for all regions except the central Transverse Ranges area, where viscoelasticity may play an important role in controlling crustal deformation. However, as *Rundle and Jackson* [1977b] and *Savage and Prescott* [1978] showed, by varying the slip

Table 4. Phase II Fault Model

Fault Segment	Latitude A, degree	Longitude A, degree	Latitude B, degree	Longitude B, degree	Dip, degree	Lock Depth, km	Strike Slip, mm/yr	Dip Slip, mm/yr
SAF North	35.978	120.529	-	-	90.0	20.0	34.0	0.0
SAF Carrizo Plain	35.978	120.529	34.783	118.807	90.0	20.0	34.0	0.0
SAF Mojave	34.783	118.807	34.278	117.477	90.0	20.0	30.0	0.0
SAF San Bernardino Mtns	34.278	117.477	34.034	116.670	90.0	20.0	24.0	0.0
SAF Coachella Valley	34.034	116.670	33.360	115.722	90.0	20.0	25.0	0.0
SAF Brawley Seismic Zone	33.360	115.722	32.931	115.550	90.0	20.0	25.0	0.0
Imperial	32.932	115.551	32.667	115.343	90.0	20.0	30.0	0.0
SAF South	32.667	115.343	-	-	90.0	20.0	45.0	0.0
SJF San Bernardino Valley	34.245	117.508	34.017	117.237	90.0	20.0	12.0	0.0
SJF San Jacinto Valley	34.017	117.237	33.740	116.917	90.0	20.0	12.0	0.0
SJF Anza	33.740	116.917	33.263	116.122	90.0	20.0	12.0	0.0
SJF Coyote Creek	33.457	116.508	33.200	116.194	90.0	20.0	4.0	0.0
SJF Borrego Mtn	33.200	116.194	33.011	115.975	90.0	20.0	4.0	0.0
SJF Superstition Mtn	32.993	115.922	32.888	115.702	90.0	20.0	4.0	0.0
SJF Superstition Hill	33.013	115.838	32.892	115.643	90.0	20.0	4.0	0.0
WEF Whittier	33.986	118.018	33.854	117.637	90.0	20.0	2.5	0.0
WEF Glen Ivy	33.854	117.637	33.643	117.348	90.0	20.0	5.0	0.0
WEF Temecula	33.643	117.348	33.377	117.013	90.0	20.0	5.0	0.0
WEF Julian	33.377	117.013	32.965	116.362	90.0	20.0	5.0	0.0
WEF Coyote Mtn	32.965	116.362	32.779	116.006	90.0	20.0	4.0	0.0
WEF South	32.654	115.823	32.382	115.468	90.0	20.0	4.0	0.0
Palos Verdes North	33.892	118.472	33.702	118.223	135.0	20.0	3.0	0.0
Palos Verdes South	33.702	118.223	33.361	117.993	135.0	20.0	3.0	0.0
San Cayetano	34.384	118.801	34.433	119.922	135.0	20.0	0.0	6.0
Santa Susana	34.384	118.801	34.271	118.443	45.0	20.0	0.0	5.0
Sierra Madre	34.271	118.443	34.147	117.871	45.0	20.0	0.0	3.0
Cucamonga	34.147	117.871	34.187	117.422	45.0	20.0	0.0	3.0
Oak Ridge	34.384	118.801	34.246	119.260	45.0	20.0	0.0	4.0
Garlock West	34.811	118.921	35.422	117.737	90.0	20.0	-5.0	0.0
Garlock East	35.422	117.737	35.587	116.330	90.0	20.0	-7.0	0.0
E CA Shear Zone South	34.144	116.197	35.422	117.737	90.0	20.0	5.0	0.0
E CA Shear Zone North	35.422	117.737	-	-	90.0	20.0	5.0	0.0
Hosgri North	36.417	122.000	-	-	90.0	20.0	3.0	0.0
Hosgri Central	36.417	122.000	35.308	120.958	90.0	20.0	3.0	0.0
Hosgri South	35.308	120.958	34.650	120.642	90.0	20.0	3.0	0.0
Offshore Islands	32.464	117.815	33.983	119.573	90.0	20.0	4.0	0.0

Dip angles measured from horizontal downward, possitive for dextral strike slips, and possitive for thrust dip slips.

rates and locking depths, an elastic half-space model could produce almost the same surface deformation as does a viscoelastic model. We use the elastic half-space model for convenience but caution the reader that our interpretation is not unique. The predicted station displacements are compared with the data, and the postfit residual χ^2 is evaluated. Two fault models are tested in our forward modeling. Model HD (for "horizontal detachment") assumes that thrust faults such as the Cucamonga fault, Santa Susana fault, San Cayetano fault, and Oak Ridge fault slip horizontally below the 20-km locking depth. This model tests the existence of a horizontal decollement suggested by cross section balancing studies of the region [*Davis et al.*, 1989; *Huftile and Yeats*, 1995; *Shaw and Suppe*, 1996]. We constrain these thrust faults to slip in the same direction, so that they do not pinch each other or leave gaps at depth. We allow the fault widths to vary in the same way simultaneously and find that the postfit χ^2 reaches a minimum when the horizontal extent of the decollement reaches about 35 km.

In model CD (for "constant dip"), we keep the dip angles of the thrust faults unchanged and assume the faults slip aseismically below the seismogenic zone. This model tests the arguments that subduction is taking place locally underneath the thrust fault zones, as suggested by seismic tomography [*Humphreys et al.*, 1984; *Humphreys and Clayton*, 1990]. However, the model itself lacks the sophistication that subduction models usually require. We use a 45° dip angle and allow the fault widths to vary. We find that the postfit residual χ^2 reaches a minimum when the fault width below locking depth reaches 42 km. Its horizontal projection is 30 km, close to 35 km extent that we estimated for model HD. Thus the thrust faults cut through the SAF at depth in both models. Although 42 km is the best estimate of the fault width, a broad range of fault widths between 42 and 60 km would fit the data almost equally well. We choose 42 km as the fault width in our model, knowing that the actual faults could extend much beyond.

Figure 5 shows the dislocation fault model of Model CD and the postfit residual velocities of the stations. Net translation of the network has been subtracted from the residual velocities. Agreement between the data and the predictions from the WGCEP fault model is very good, considering that the WGCEP fault model is mainly geological with little input from geodesy. This observation suggests that present-day deformation is dominated by slip along faults whose present-day slip rates do not differ significantly from their averages over thousands or even hundreds of thousands of years. Nevertheless, there are still systematic differences at a few regions, which will be our focus below.

The residual velocity vectors show three prominent features. First is an apparent NW-SE extension, observable from the fact that the stations in the top left part of the diagram have residual velocities to the NW, and stations in the bottom right have SE residual velocities. The magnitude of these residual velocities generally increases with distance from the geographical center of the stations. The second feature is an apparent left-lateral shear across the Mojave section of the SAF and the Sierra Madre-Cucamonga fault system. The third feature is an apparent right-lateral shear across the southern San Jacinto fault. The last two features, however, are correlated with and could be partially explained by the first feature.

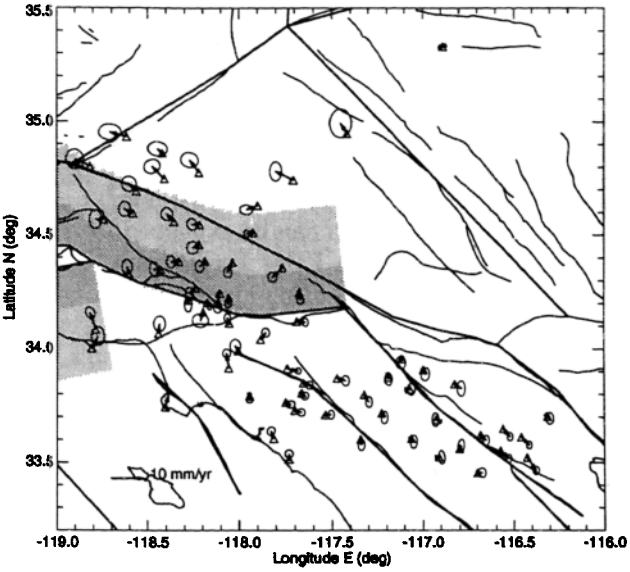

Figure 5. Station residual velocities. Solid lines are the fault patches whose parameters are given in Table 4. The dark grey and light grey regions are the surface projections of the locked and deeper deforming sections of the thrust faults, respectively. Velocity residuals are the velocity solutions minus the WGCEP model-predicted station velocities. Error ellipses are one standard deviation.

The residual extension may be a natural reaction to the NNE-SSW contraction across the Los Angeles basin and San Gabriel Mountains. The contraction built into the WGCEP model is produced by thrust faulting which balances the horizontal shortening by thickening in the vertical direction. However, the model features no corresponding extension that would prevent horizontal areal contraction. In other words, the crust may be responding to the NNE-SSW contraction in a way not incorporated into the WGCEP model.

The residual shear strain rate on the SJF could result from underestimating the right-lateral slip or using an inadequate locking depth along the SJF in the WGCEP model. Seismicity along the southern section of the fault [*Webb and Kanamori*, 1985; *Jones*, 1988; *Hill et al.*, 1990] shows a shallower profile (< 15 km) than that of the northern section, suggesting that adjusting the locking depth of the WGCEP model may improve the fit and also help reduce the apparent NW-SE extension.

In the SW part of the network, station PVER moves about 3 mm/yr more northerly than the WGCEP model

predicts with respect to the sites between the Whittier-Elsinore fault and the Palos Verdes fault. Part of this discrepancy could be blamed on limited mapping of the Palos Verdes fault in the WGCEP model. Had the fault been mapped farther along its NW and SE ends, the discrepancy could be reduced by half or so. Stations CATO and PTDU also show 3-5 mm/yr residual northward motion, which can be explained by a lack of NW continuation of the Palos Verdes fault, or by the absence of convergent faulting along the Malibu-Santa Monica fault system in the WGCEP model, or by insufficient thrust motion along the Oak Ridge fault system in the WGCEP model, or by a combination of the three. There is about 4 mm/yr NNW residual velocity at station LANW. Further continuation of the Whittier fault from its current NW end may help reduce the discrepancy, but we cannot rule out the possibility that the velocity solution is corrupted by unreliable local ties for the triangulation stations at the site as we discussed earlier. In the NE part of the network, residual velocities between MOJA and HAWE show a slightly right-lateral slip pattern, which could be reduced by more dextral slip along the Mojave Shear Zone than the 5 mm/yr placed by the WGCEP model.

The residual shear strain rate on the Mojave section of the SAF could result from using inadequate fault parameters for the SAF in the WGCEP model, or using an elastic dislocation model which is inadequate itself as discussed earlier. A number of models are tested to explore the first possibility. By altering the locking depth and the slip rate along that section of the fault, we find a maximum reduction of about 8% to the postfit residual χ^2, achieved by a model with 30-km locking depth and 30-mm/yr slip rate (Table 5). If the locking depth is fixed at 20 km, the best fit fault slip rate is about 25 mm/yr, but the postfit χ^2 reduction is less significant than in the case of depth variation. We think the 30 mm/yr slip rate is probably closer to the truth. The 30-km fault locking depth may not mean that the fault is locked that deep but may imply a broader distribution of the wrench-style deformation than a reasonable elastic half-space fault model would predict. Such broad deformation may be caused by detachment or viscoelastic motion in the lower crust or upper mantle around the Mojave section of the SAF.

We test also a case of greater slip rate along the Eastern California Shear Zone than the WGCEP model predicted. A minimum postfit residual is obtained at a rate of 8 mm/yr for model HD and 6 mm/yr for model CD. The improvements to the two thrust-fault models are significant at 64% and 35% confidence levels, respectively. The confidence levels are determined based on the F test, which tests the significance of introducing new model parameter(s) to improved model fitting. In the tests given above and a number of other tests listed in Table 5, the input data have 132 degrees of freedom, the base model has zero degree of freedom in the parameter space, and the model being tested usually has 1 degree of freedom.

Using a modified WGCEP model with 30-km locking depths for the Mojave section of the SAF and 6-8 mm/yr right-lateral shear along the Eastern California Shear Zone, we find about 1-4 mm/yr WNW residual motion left for the sites in the San Gabriel Mountains and the western Mojave desert. Although modest, this motion appears to be systematic. We showed earlier that thrust motion or decollement under the San Gabriel Mountains may explain the N-S contraction in the region. The same mechanism, coupled with oblique slip across the detachment, could explain the WNW mo-

Table 5. Solution Statistics

SAF		ECSZ	Thrust Faults			
Lock Depth, km	Dextral Slip, mm/yr	Dextral Slip, mm/yr	Width, km	Sinistral Slip, mm/yr	Residual χ^2	Confidence, %
		Horizontal Decollement Model (Model HD)				
20	25	5	35	0	698.2	
20	30	5	35	0	732.9	
30	30	5	35	0	686.9	99.6
30	30	8	35	0	682.5	64.2
30	30	8	35	6	653.9	98.2
		Constant Dip Model (Model CD)				
20	25	5	42	0	685.1	
20	30	5	42	0	724.3	
30	30	5	42	0	669.0	99.9
30	30	6	42	0	667.9	34.9
30	30	6	42	13	615.8	99.9

Each model confidence level is obtained from comparing the model with the one above it.

tion of the block. Allowing a uniform left-lateral slip component along the Cucamonga fault, Sierra Madre fault, Santa Susana fault, and San Cayetano fault, we find the best fit to the data when the left-lateral slip equals 6 mm/yr for the model HD and 13 mm/yr for the model CD, respectively. The model improvements are at 99% confidence for both models. The left-lateral slip along the thrust faults could be lower than 13 mm/yr depending on how the motion direction is defined. We define N-S motion as normal and E-W motion as lateral. The definition is precise for the Cucamonga fault, San Cayetano fault, and the east portion of Sierra Madre fault, but not so for the Santa Susana fault and the west portion of Sierra Madre fault which strikes about 28° clockwise from the strike of Cucamonga fault. If we evaluate the lateral motion parallel to the strike of the Santa Susana fault, the left-lateral slip for model CD at the thrust fault surface is about 9 mm/yr. The residual velocities of the modified model CD are shown in Figure 6 and listed in Table 3. Significant along-strike motion of the thrust faults can be interpreted as the result of shear motion across the SAF. We will discuss in more detail the mechanisms of this along-strike motion along the thrust faults.

Strain Rate Analysis

Strain Rate Modeling Method

While station velocity diagrams demonstrate relative motions among stations, strain rate diagrams show in situ strain concentration rates which connect directly to local stress concentration rates and possibly to seismic hazard potentials [*Ward*, 1994]. We derive strain rates from the velocity estimates given above.

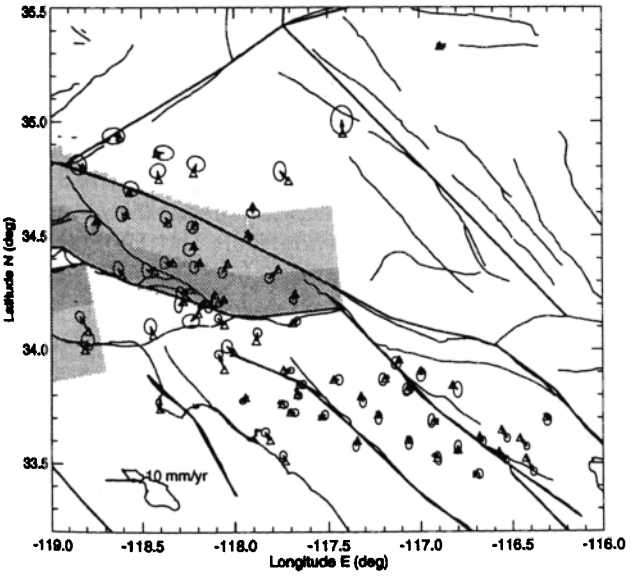

Figure 6. Same as Figure 5 but with revised fault parameters along the Mojave section of the SAF, the ECSZ, and the thrust faults beneath the SGM for station velocity prediction. See text for detail.

This method, like most previous methods [e.g., *Frank*, 1966; *Prescott*, 1976], interpolates the strain rates using discretized geodetic measurements. However, unlike other previous methods, this one models strain rates as continuous functions within the entire network. At each location, a uniform strain rate field is assumed, a least squares inversion is performed over the station velocity solutions and their covariances to solve for six parameters: the velocity components U_x and U_y, rotation rate w, and strain rate components τ_{xx}, τ_{yy}, and τ_{xy}. Other commonly used strain terms, such as the maximum shear strain rate τ_{max} and the dilatation rate τ_{dil} can be derived afterward from the three strain rate components. The modeling algorithm can be written in the following form:

$$\begin{pmatrix} V_x^I \\ V_y^I \end{pmatrix} = \begin{pmatrix} 1 & 0 & \Delta x_I & \Delta y_I & 0 & \Delta y_I \\ 0 & 1 & 0 & \Delta x_I & \Delta y_I & -\Delta x_I \end{pmatrix} \begin{pmatrix} U_x \\ U_y \\ \tau_{xx} \\ \tau_{xy} \\ \tau_{yy} \\ w \end{pmatrix} + \begin{pmatrix} \epsilon_x^I \\ \epsilon_y^I \end{pmatrix}$$

where V_x^I and V_y^I are the observed Ith station velocity components at a location $\vec{r}_I$. All variables on the right hand side of the equation are to be evaluated at a location $\vec{R}$, Δx_I and Δy_I are the vector components of $\Delta\vec{R}_I = \vec{r}_I - \vec{R}$. The 2×6 matrix is the partial derivative matrix and ϵ_x^I and ϵ_y^I are the errors of the corresponding velocity components. The covariance matrix for ϵ_x^I and ϵ_y^I is E_{ij} which is a weighted version of C_{ij} used for constructing the local averages. C_{ij} is the covariance matrix of the velocity estimation errors obtained from our geodetic data adjustment. The weighting is given as

$$E_{ij} = C_{ij} \exp \frac{\Delta R_I^2 + \Delta R_J^2}{\sigma_D^2}$$

where i and j are the velocity components corresponding to the Ith and the Jth stations, ΔR_I and ΔR_J the distances from the Ith and the Jth stations to the spot to be estimated, and σ_D is a distance-decaying constant, taken as 25 km. This weighting means that a station 20.8 km away from the spot to be evaluated will contribute only one-half its unweighted value to the velocity solution. The contribution is reduced to 14% if the station is 35 km away. To save computation time, we exclude stations from the least squares inversion if the distance exceeds 50 km and the calculated contribution would be less than 2%. This algorithm has certain advantages. The major one is that the model represents the strain rate field in a realistic way; i.e., for a local region of about 20 km in diameter the strain rate field is quasi-uniform; but for a region of 100 km in diameter the strain rate field varies continuously. Our strain rate estimates are less biased because of proper weighting, and they are stable because they are evaluated as

weighted averages over the region. Strain uncertainties can also be derived.

Strain Rate Results

Figures 7 and 8 illustrate the strain rates in the region. Figure 7 shows the maximum shear strain rates and directions, and Figure 8 shows the principal strain rates and axes. The strain rates are plotted only when the solutions reach a reasonable level of confidence (uncertainties less than 0.15 μstrain/yr). A number of features are found from the strain distributions:

1. The maximum shear strain rates distribute along three faults: the SAF, SJF, and Sierra Madre-Cucamonga fault system. It is no surprise to see significant shear strain rates along the first two faults, known to have the greatest slip rates of all faults in southern California. For the Sierra Madre-Cucamonga fault system, however, a dextral shear strain rate of 0.20 $\pm$ 0.03 μrad/yr oriented N45°W newly reveals that it is probably the thirdmost geodetically active fault system in the region whose shear strain rates are resolved here, with N-S compression and E-W extension about equally active. The maximum shear strain rates in the San Gabriel Mountains are quite close to 0.13 μstrain/yr striking N63°W determined by *Savage and Lisowski* [1994].

2. The maximum convergence strain rates (Figure 8) seem to reach peaks at the westernmost Mojave desert near the GF and along the SJF close to its triple junction with the Banning fault. Such high convergence rates could be interpreted as local SSE convergence near the White Wolf fault and as N-S convergence near the Banning fault. However, the reliability of the estimated convergence there may be questioned, as the two maxima are located at the boundaries of our network. A compressional belt runs from the Sierra Madre-Cucamonga fault system to the Raymond Hill fault and

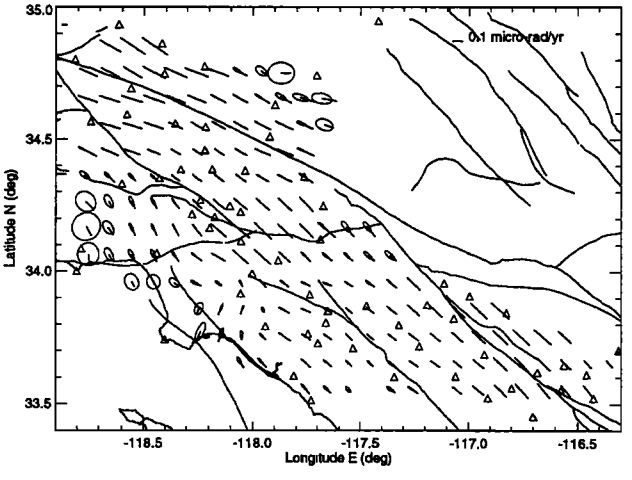

Figure 7. Horizontal maximum shear strain rates. The amount and direction of the maximum shear strain rates are shown by arrows with error ellipses representing one standard deviation. The open triangles denote the station locations.

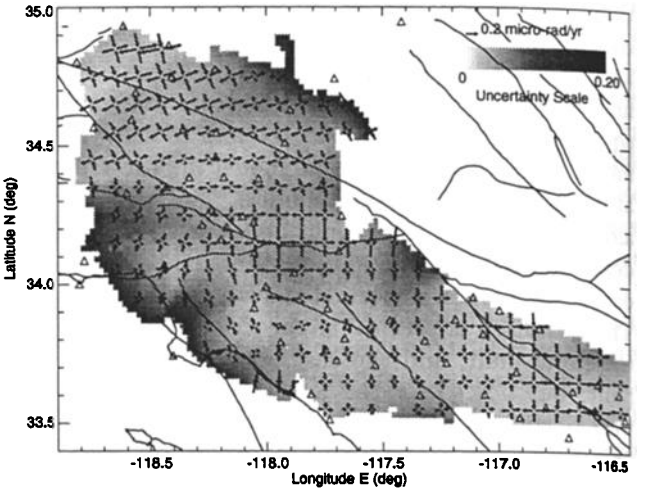

Figure 8. Horizontal principle strain rates. The amount and direction of the principle strain rates are shown by arrows with their uncertainties represented by the degree of greyness in the region where the principle strain rates are resolved. The open triangles denote the station locations.

Santa Monica fault, where the N-S compressional rate ranges from 0.12 to 0.22 μstrain/yr. This compressional belt has produced several moderate-sized thrust earthquakes during the last decade, including the 1987 M 5.9 Whittier Narrows and 1991 M 5.8 Sierra Madre earthquakes. The 1971 M 6.6 San Fernando and the 1994 M 6.7 Northridge quakes are located close to but not within this high compressional strain belt. The western section of the compression belt has been previously identified as the northern flank of the Elysian Park fold and thrust system [*Hauksson*, 1990]. *Hauksson* [1990] reported that the compressional axes of the earthquakes had a systematic trend from a N-S direction east of the Los Angeles basin to NNE west of the basin. This pattern seems consistent with our study.

3. South of the Los Angeles basin, our velocity solutions show that strike-slip motions dominate. From the Newport-Inglewood fault to the SJF, the region undergoes a deformation of about equal amounts N-S compression and E-W extension, from about 0.1 μstrain/yr along the Newport-Inglewood fault and Elsinore fault to about 0.2 μstrain/yr along the SJF. This result is consistent with the finding by *Johnson et al.* [1994], who studied strain rates in the Anza trilateration network using the same set of EDM data that we use here. The maximum shear strain rates are relatively low in the Los Angeles basin and the San Fernando valley; the maximum convergence rates are low at the center of the San Gabriel Mountains, San Fernando valley, and south of the Los Angeles basin.

4. Virtually no extension is found from the SW foothills of the San Gabriel Mountains to the coast, a region that includes the Santa Susana fault and Santa Monica fault. The region therefore shows some areal contraction. The amount of horizontal areal contrac-

tion rate might indicated active thrusting and orogeny taking place in such environments.

5. There is about 0.14 μstrain/yr E-W extension at the northern tip of the Whittier fault. Such extension is possibly caused by the bifurcation of the Whittier fault and the Elsinore fault and by the local ending of the Whittier fault there. This notion makes sense because the station postfit residuals of the WGCEP model are small in the region except for LANW. However, we do not want to overinterpret the results there since the velocity solutions for the sites in the region are probably weaker than for other sites.

Rotation rates for the network are shown in Figure 9. Large rotation rates are found along the SAF and the SJF, as expected from active wrenching dislocations along the two faults. Of interest is the rotation pattern's elliptical high around the center of the Mojave section of the SAF, with the maximum located about 10 km north of the fault. An initial interpretation for this rotation pattern could be that the San Gabriel Mountains has a distinct rotation compared to its south and west neighbors: the San Gabriel Mountains moves like a solid block. However, a close examination of the postfit residuals in Figure 6 shows no systematic rotation pattern left in this region, indicating that the concentrated rotation rate in the region has been explained by the model, in which the SAF, the oblique-thrust faults, and the Garlock fault all play important parts. We choose not to show the translation rates, because they resemble roughly the original velocity field as shown in Figure 4.

Discussion

Various models for crustal deformation have been developed for southern California. *Bird and Rosenstock* [1984] modeled the crustal deformation as relative motion among subblocks bounded by faults. Using the geologically determined fault slip rates available at the time, they inverted the subblock motions. One remarkable feature of their model is strong convergence along the Cucamonga-Sierra Madre-Santa Susana fault system. They proposed a model with almost vertical subduction underneath the central Transverse Ranges area. A model proposed by *Weldon and Humphreys* [1986] based on geological evidence reduced the convergence at the Cucamonga fault to about 3 mm/yr and argued that major convergence was transferred to the west along faults in the Ventura basin region. A subsequent finite element model by *Saucier and Humphreys* [1993] followed up this idea and incorporated other regional faults to describe the deformations in more detail. These previous studies revealed important features but suffered from sparse and sometimes inaccurate data available then. There were few reliable data to pin down the motion along the Mojave section of the SAF. Moreover, there were problems with the plate motion velocity estimate between the Pacific and the North America plates and with the convergence rate at the Ventura basin.

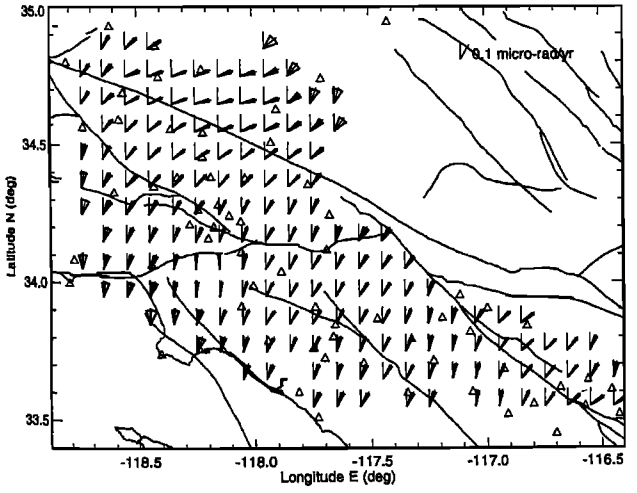

Figure 9. Rotation rates. The amount of the rotation rates is measured from north with cone shaped error ranges to represent one standard deviation. The open triangles denote the station locations.

Our study fills an observational gap along the Cucamonga-Sierra Madre-Santa Monica fault system, so that we can better understand interactions between the San Gabriel Mountains and the Los Angeles basin. Convergence is significant only at the northern part of the basin. N-S convergence is accommodated mainly along the Cucamonga-Sierra Madre-Santa Susana and Santa Monica-Raymond Hill fault systems.

Two important observations suggest the abnormal behaviors of the San Gabriel Mountains. The first one shows that the deformation across the block along a profile normal to the SAF is broader than would be predicted by an elastic dislocation model with reasonable locking depth and slip rate parameters of the SAF. This finding implies that the displacements beneath the upper crust cannot be described as slip between two elastic blocks, but rather as shear motion across a broad deformation zone. The second observation is that the San Gabriel Mountains and the SW Mojave desert move about 3 mm/yr WNW with respect to the southern region. Such motion might be part of a NW-SE extension across the SJF and the Mojave section of the SAF caused by NE compression in the central Transverse Ranges area. Alternatively, it might be the result of left-lateral oblique thrust underneath the San Gabriel Mountains and possibly the SW Mojave desert, with the topmost crust being peeled off the upper mantle base. Although previous geological studies revealed that such blind thrust motions could happen [*Davis et al.*, 1989; *Dolan et al.*, 1995] they could not determine exactly the direction and extent of the motions (e.g., whether penetrating the SAF). A trenching study at the Cucamonga fault [*Morton and Matti*, 1987] showed no oblique component for the thrust fault. However, this may not directly contradict to our model, since the

oblique motion might not be significant until the material thrusts to certain depth.

Seismological studies have revealed that the San Gabriel Mountains do not have a significant root [*Hadley and Kanamori*, 1977; *Sung and Jackson*, 1992]. The observation could be explained by having a horizontal decollement underneath the mountains which would shift the plate boundary to the east north of the Big Bend. Although such a scenario is possible, however, no one has offered a quantitative deformation model. If our thrust or oblique-thrust model is valid, the thrusts of the Cucamonga-Sierra Madre system may eventually cross the SAF as shown in Figures 5 and 6. If the oblique-thrust model holds, a left-lateral motion along the faults might be as large as 10 mm/yr. This might occur if the San Gabriel Mountains were glued by friction to the Mojave desert block, at least in the upper crust and between earthquakes, but separated from the lower crust by a detachment surface. Relative motion across this thrust ramp might be caused by horizontal compressive stress along the Cucamonga system, preventing the San Gabriel Mountains and the SW Mojave block from keeping up with the southeastward motion of the Mojave block, resulting in a delay of the lateral motion of the upper block with respect to the lower block. For the surface mass transport in the San Gabriel Mountains region, our oblique-thrust model supports the kinematic model of *Weldon and Humphreys* [1986] but differs from it in describing the deformation at depth.

Figure 10 is a cartoon of our kinematic model. In the model the Mojave section of the SAF is intersected at depth by the north dipping thrust faults, making the San Gabriel Mountains a sliver block deformed both by thrust motion underneath and lateral shear on the NE. It is still problematic if the SAF is cut off completely or partially by the thrust faults beneath its surface trace and how far (if any) the SAF is shifted NE at depth. An altered or shifted boundary zone beneath the surface expression of the SAF would support *Snay et al.*'s [1996] finding that the major deformation band at the Big Bend region is wider than that at the Carrizo plain section of the SAF and is oriented about 7° clockwise relative to the surface trace of the SAF.

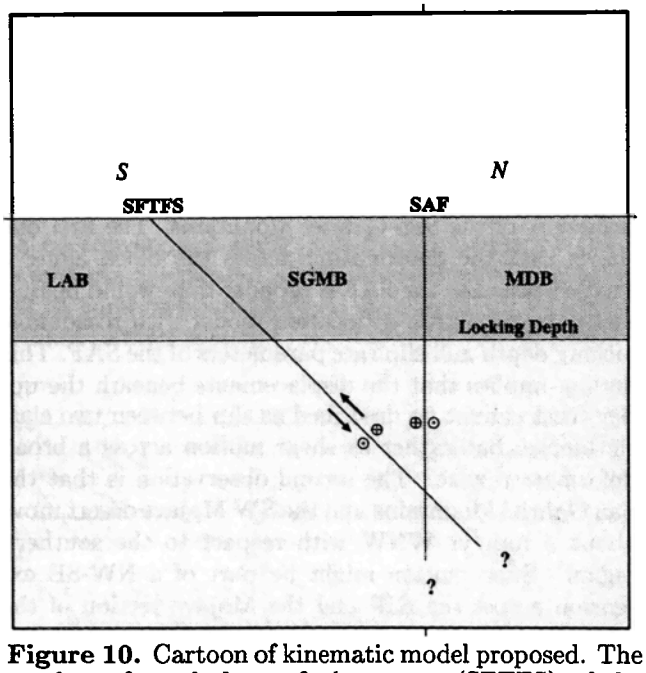

Figure 10. Cartoon of kinematic model proposed. The southern frontal thrust fault system (SFTFS) of the SGM subducts beneath the SGM and intersects with the SAF at depth. Arrow and circle pairs indicate the relative motion direction at fault-plane surfaces; circled dot indicates relative motion toward the reader, and circled cross indicates motion away from the reader. The compression along the Cucamonga fault causes excessive WNW motion of the San Gabriel Mountains block, producing left-lateral shear on the thrust ramp at depth. The extent and direction of the thrust faults beyond the SAF and the location of the SAF below its intersection with the thrust faults are not resolved in this study.

Conclusions

In modeling a full pallette of geodetic data collected in the Los Angeles basin and vicinity, we have derived 66 independent interseismic station velocities accurate to within a couple of millimeters per year. Our interpretations of the velocities lead to following conclusions.

1. The fault model provided by the Southern California Earthquake Center earthquake probability report [*WGCEP*, 1995] describes the crustal deformation in general; i.e., crustal deformation is apparently dominated by a few major faults in southern California, such as the SAF, SJF, Garlock fault, and Eastern California Shear Zone.

2. Significant convergence and shear motion occur along the southern frontal fault system of the San Gabriel Mountains. The shear motion rate along the Sierra Madre-Cucamonga fault system is the third largest behind the SAF and the SJF within the central Transverse Ranges and Peninsular Ranges.

3. After removing the velocity field predicted by the WGCEP model, residual velocities show systematic patterns in the San Gabriel Mountains area and along the southern SJF. Some residuals can be explained by adjusting the WGCEP model along the SAF and SJF. Others can be explained by either a NW-SE extension caused possibly by NE-SW compression in the region or a left-lateral oblique thrust along an extension of the Cucamonga-Sierra Madre thrust system.

4. Low strain rates are found along the Elsinore fault and Newport-Inglewood fault. N-S compression decreases from the Raymond Hill fault westward to the Santa Monica fault, and the maximum compression direction rotates gradually from north in the east section to NNE in the west section. The San Fernando valley is being compressed N-S with little E-W extension.

Appendix: Station Evolutions and Local Ties

ANTO. Main station Antonio 1923 (ANTO) has been measured using GPS. One of its auxiliary stations, Antonio Aux, about 20 m north from the main station, has been surveyed by trilateration. Their local distance tie is used here. Their azimuthal tie is not used because of doubts concerning its integrity.

CATO. Main station Castro 1898 (CAT0) is difficult to observe using GPS because of strong radio interference. A GPS occupation has been made at another site, Solstice Cyn B2 Aux 1 (CATO), about 14 m south of CAT0. A GPS tie was made between the two sites in 1990. Another site, Castro 1898 Rm 3 (CAT3), has been measured in triangulation surveys along with CAT0 and is tied to CAT0 locally. CAT3 is also included in this study.

ECHO. Main station Echo Rock 1933 (ECHO) has been repeatedly observed using GPS since 1987. A reference mark, Echo Rock Rm 2 (ECH2), was measured with GPS in 1990 and tied to ECHO later. Their velocities are assumed equal.

JPLM. Three GPS stations are used in this study. JPL Aries 1 1975 (JPLA), JPL Aries 1 1975 Rm 1 (JPLR), and JPL MESA (JPLM). JPLM has been observed since 1990 and is used as a fiducial station in southern California. This site has been tied to the other two sites with GPS. JPLA and JPLR have also been measured in USGS trilateration surveys.

LANW. The original triangulation site Los Angeles NW Base 1889 (LAN0) was destroyed in the late 1950s or early 1960s. A distance between this station and station Los Angeles NW BS 2 1956 (LAN2) was measured, and angles involving the two stations plus a remote site, SPE0, were observed in the 1950s. After the destruction of LAN0, LAN2 was subsequently observed in triangulation surveys in the 1960s, sometimes involving another local station, LA NW BS Aux 3 1964 (LAN3), which now has been occupied using GPS. All the local measurements are used to tie LAN0 to the GPS station at the site, although the local ties are not that accurate. The postfit uncertainty for LAN0 is about 50 mm for the two horizontal components. Another station, Whittier D11 (WD11), was located about 1 km west, measured using GPS, and intended as a substitute for LAN0. However, this station was lost after two epochs of measurements in 1989 and in 1991. The station velocity of WD11 is assumed equal to the station velocity of LANW in this study.

LASE. Main station Los Angeles SE Base 1889 1957 (LASE) is seated in a courtyard of a private residence. This station was reset in 1957. Comments in the LA County Survey Control Station Description referred to the new marker's "geographic position remaining unchanged." Our assumption is that the marker was reset faithfully to its original horizontal position within a few millimeters.

MICH. Main station Michelson 1923 (MICH) still exists but is covered by heavy foliage which makes GPS occupation difficult. A GPS tie was made between one of its reference markers, Rm 1 (MIC1), and ECHO. This tie has been used along with local tie measurements between MICH and MIC1 to link MICH to ECHO.

MOJA. Several GPS stations have been used as fiducial stations at Goldstone, Mojave. The early ones were MOJA, using a TI4100 antenna; MOJF, a FRPA-2 antenna; and MOJM, a MiniMac antenna. A TurboRogue station DS10 has been in operation since 1990 but is located about 10 km north of the other three. Unfortunately, no reliable ties exist between the early three that we know of (problems may exist for the vertical components of the local ties; see appendix of *Feigl et al.* [1993]. There are GPS ties between MOJM and DS10. In this study we tie the velocities of the four stations together but make no local ties between them except for the GPS ties between MOJM and DS10.

NIGU. Main station Niguel 1884 (NIG0) was destroyed in the early 1980s. There is no reliable tie between this station and our GPS station Niguel A 1981 (NIGU), hundreds of meters away. In this study we tie only the two station velocities together.

PINY. An early GPS occupation at the site was made at station Pinyon Flat NCMN 1981 (PINY). Since 1990, a permanent station, PIN1, was established as a local fiducial station, although different antenna types have been used at the site. We use data from both stations and tie their velocities together.

PSEB. A local station, Pasadena East Base 2 1922 (PSE2), is about 80 m from the main station Pasadena East Base 1922 (PSEB). PSE2 has also been surveyed during some of the triangulation experiments. This site and the corresponding data are included in this study; its velocity is tied to PSEB.

SAFE. Main station San Fernando 1898 (SAF0) was destroyed in the late 1950s. An existing mark, San Fernando 1898 Aux 3 (SAF3), was also observed in some of the triangulation surveys and SAF3 is about 22 m from SAFE and tied to it locally. GPS occupations have been made at two sites: San Fernando Aux 2 Ecc 1 Rm 2 1967 (SAFE) and PICO NCER 1977 (PICO). Station PICO is also a USGS trilateration site. SAFE has been tied to SAF3 and PICO separately using GPS, and the uncertainty of the tie between SAFE and SAF0 is estimated to be about a couple of centimeters.

SNTZ. Main station Covina C7 San Tuze 1957 (SNT0) was reset in 1957 in a mass of concrete, but the mark was lost in 1987. The first GPS survey of the site was made at one of its reference marks, Rm 1 (SNTZ). The main mark was reset in a large concrete mass in 1991 and stamped Johnson Frank Assoc., GPS Station, Covina C7, San Tuze 1957, Reset 1990. A local tie between the reset mark and SNTZ was made using GPS. The reset we believe should be within a few millimeters of its original horizontal position.

SPE0. The original triangulation station San Pedro 1853 1880 (SPE0) still exists, but strong radio interference from an array of microwave antennae nearby makes GPS occupation difficult. A local tie recovered from a LA City Engineering survey control map to the GPS observed reference station, Rm 2 (SPED), is used here. The tie is believed precise at the millimeter level.

UCLA. Two GPS stations (UCLA and UCL0) are used in this study. They are located atop two buildings and are about 42 m apart. A local tie between the two sites was made using GPS.

WILP. Main station Wilson Peak 1890 (WILP) was demolished in the late 1950s. There is no local tie for this station to any other locally existing station. However, stations Echo Rock 1933 (ECHO) and Michelson 1923 (MICH) are also located atop Mount Wilson, and a number of triangulation measurements were made to the three sites from other remote sites in the past. These measurements provide somewhat weak ties between the three. ECHO and MICH are about 600 m and 700 m away from WILP, respectively. Because all three are bedrock sites, we assume that there has been no relative motion between them. Velocity ties are made between the three in this study.

WORK. Main station Workman Hill 1932 (WORK) was reset in 1978 and again in 1989. The 1987 Whittier Narrows earthquake may have also perturbed the site by a centimeter or so. Our first GPS observations were made right after the 1987 quake. Our 1989 measurements were made after the 1989 reset. Although the reset by a crew from LA City was claimed accurate, modeling of displacement at the site raises some doubt. In this study we ignore the 1987 GPS measurements at the site and treat the two resets and the 1987 coseismic effect as one unknown jump.

Acknowledgments. We are very grateful to Michael Cline, who organized the 1992 Southern California Earthquake Center Gorman GPS experiment and made the data available to this study. He also reviewed the manuscript carefully and offered many useful suggestions. We also thank David Potter and Steven Salyards for their time-consuming efforts devoted to archiving the GPS data. Yanjie Feng processed part of the GPS data. Li-yu Sung, Peng Fang, Mercedes Kim, Chris Mills, and Mark Martins helped to collect part of the GPS data. We thank all the people who participated the "Trex" surveys from 1986 to 1991 and some extended surveys afterward; particularly, Andrea Donnellan for the data she collected at Castro Peak and Oat Mountain. This study also used data from eight sites measured during the 1993 Inter-county survey, organized by Ken Hudnut, and we owe special thanks to him. We thank Richard Snay, who kindly provided us the historical triangulation data, the valuable information about the Michelson baseline, and the algorithm converting the taped distances. We thank the GAMIT authors, particularly Bob King, Yehuda Bock, and Tom Herring for making the software available to us. We thank Yehuda Bock and Peng Fang, who made the PGGA daily solutions available to us. Peng Fang's countless briefings and answering of our data processing questions are especially appreciated. We are also grateful to Danan Dong for the discussions about the reduction of the trilateration data and the local ties between the trilateration and GPS. Kathy Jackson's careful review of the manuscript is especially acknowledged. Ken Hudnut and Brad Hager's comments greatly helped improve the manuscript. Several figures were plotted using the GMT software [*Wessel and Smith*, 1991]. This work has been supported by the National Science Foundation through grant EAR86-18393, U.S. Geological Survey through grants 14-08-0001-G1956 and 1434-94-G2497, and the National Science Foundation, the U.S. Geological Survey, through the Southern California Earthquake Center, grants 608816 and 566259. Southern California publication 250.

References

Argus, D. F., and R. G. Gordon, No-net-rotation model of current plate velocities incorporating plate motion model NUVEL-1, *Geophys. Res. Lett., 18*, 2039-2042, 1991.

Atwater, T., Plate tectonic history of the northeast Pacific and western North America, in *The Geology of North America*, vol. N, *The Eastern Pacific Ocean and Hawaii*, edited by Winterer, E. L., D. M. Hussong, and R. W. Decker, pp. 21-72, Geol. Soc. of Am., Boulder, Colo., 1989.

Biasi, G. P., and R. Weldon II, Quantitative refinement of calibrated 14C distributions, *Quat. Res., 41*(1), 1-18, 1994.

Bird, P., and R. W. Rosenstock, Kinematics of present crust and mantle flow in southern California, *Geol. Soc. Am. Bull., 95*, 946-957, 1984.

Bomford, G., *Geodesy*, 4th ed., Oxford Univ. Press, New York, 1980.

Bowie, W., Comparison of old and new triangulation data in California, in *Reports on Geodetic Measurement of Crustal Movement, 1906-71*, pp. 1-50, Natl. Geod. Surv., Silver Spring, Md., 1972.

Campbell, R. H., and R. F. Yerkes, Cenozoic evolution of the Los Angeles basin area-Relation to plate tectonics, in *Aspects of the Geologic History of the California Continental Borderland, Misc. Publ. 24*, edited by D. G. Howell, pp. 541-558, Pac. Sect., Am. Assoc. of Pet. Geol., Los Angeles, Calif., 1976.

Carter, W. E., J. E. Pettey, and W. E. Strange, The accuracy of astronomic azimuth determinations, *Bull. Geod., 52*, 107-113, 1978.

Cheng, A., D. D. Jackson, and M. Matsu'ura, Aseismic crustal deformation in the Transverse Ranges of southern California, *Tectonophysics, 144*, 159-180, 1987.

Cline, M. W., R. A. Snay and E. L. Timmerman, Regional deformation of the Earth model for the Los Angeles region, California, *Tectonophysics, 107*, 10,279-10,314, 1984.

Crowell, J. C., Problems concerning the San Andreas fault system in southern California, in *Proceedings of the Conference on Tectonic Problems of the San Andreas Fault System*, edited by R. L. Korach and A. Nur, *Stanford Univ. Publ. Geol. Sci., 13*, 125-135, 1973.

Davis, T. L., J. Namson, and R. F. Yerkes, A cross-section of the Los Angeles area: Seismically active fold and thrust belt, the 1987 Whittier Narrows earthquake, and earthquake hazard, *J. Geophys. Res., 94*, 9644-9664, 1989.

Dolan, J. F., K. Sieh, T. K. Rockwell, R. S. Yeats, J. Shaw, J. Suppe, G. J. Huftile, and E. M. Gath, Prospects for larger or more frequent earthquakes in the Los Angeles metropolitan region, *Nature, 267*, 199-205, 1995.

Dong, D. N., and Y. Bock, Global Positioning System network analysis with phase ambiguity resolution applied to crustal deformation studies in California, *J. Geophys. Res., 94*, 3946-3966, 1989.

Donnellan, A., B. H. Hager, R. W. King, and T. A. Herring, Geodetic measurement of deformation in the Ventura basin region, southern California, *J. Geophys. Res., 98*, 21,727-21,739, 1993.

Eberhart-Phillips, D., M. Lisowski, and M. D. Zoback, Crustal strain near the Big Bend of the San Andreas fault: Analysis of the Los Padres-Tehachapi trilateration networks, California, *J. Geophys. Res., 95*, 1139-1153, 1990.

Ehlig, P. L., Geologic framework of the San Gabriel mountains, *Bull. Calif. Div. Mines Geol., 196*, 7-18, 1975.

Ehlig, P. L., K. W. Ehlert, and B. M. Crowe, Offset of the Upper Miocene Caliente and Mint Canyon Formations along the San Gabriel and San Andreas faults, in *San Andreas Fault in Southern California*, edited by J. C. Crowell, *Spec. Rep., Calif. Div. Mines Geol., 118*, 83-92, 1975.

Feigl, K. L., et al., Measurement of the velocity field of central and southern California, 1984-1992, *J. Geophys. Res., 98*, 21,677-21,712, 1993.

Frank, F. C., Deduction of Earth strains from survey data, *Bull. Seismol. Soc. Am., 56*, 35-42, 1966.

Gergen, J. G., The new adjustment of the North American Datum: The observables, *Am. Congr. Surv. Mapp. Bull., 51*, 9, 1975.

Gilbert, L. E., C. H. Scholz, and J. Beavan, Strain localization along the San Andreas fault: Consequences for loding mechanisms, *J. Geophys. Res., 99*, 23,975-23,984, 1994.

Hadley, D., and H. Kanamori, Seismic structure of the Transverse Ranges, California, *Geol. Soc. Am. Bull., 88*, 1469-1478, 1977.

Hauksson, E., Earthquakes, faulting, and stress in the Los Angeles Basin, *J. Geophys. Res., 95*, 15,365-15,394, 1990.

Hearn, T. M., and R. W. Clayton, Lateral velocity variations in southern California, II, results for the lower crust from P_n waves, *Bull. Seismol. Soc. Am., 76*, 511-520, 1986.

Hill, D. P., J. P. Eaton, and L. M. Jones, Seismicity, 1980-1986, in *The San Andreas Fault System, California*, edited by R. E. Wallace, *U.S. Geol. Surv. Prof. Pap., 1515*, 115-151, 1990.

Huftile, G. J., and R. S. Yeats, Convergence rates across a displacement transfer zone in the western Transverse Ranges, Ventura basin, California, *J. Geophys. Res., 100*, 2043-2067, 1995.

Humphreys, E. D., R. W. Clayton, and B. H. Hager, A tomographic image of mantle structure beneath southern California, *Geophys. Res. Lett., 11*, 625-627, 1984.

Humphreys, E. D., and R. W. Clayton, Tomographic image of the southern California mantle, *J. Geophys. Res., 95*, 19,725-19,746, 1990.

Humphreys, E. D., and R. J. Weldon II, Deformation across the western United States: A local estimate of Pacific-North America transform deformation, *J. Geophys. Res., 99*, 19,975-20,010, 1994.

Jackson, D. D., The use of a priori data to resolve the nonuniqueness in linear inversion, *Geophys. J. R. Astron. Soc., 57*, 137-157, 1979.

Jackson, D. D., and M. Matsu'ura, A Bayesian approach to nonlinear inversion, *J. Geophys. Res., 90*, 581-591, 1985.

Johnson, H. O., D. C. Agnew, and F. K. Wyatt, Present-day crustal deformation in southern California, *J. Geophys. Res., 99*, 23,951,23,974, 1994.

Jones, L. M., Focal mechanisms and the state of stress on the San Andreas fault in southern California, *J. Geophys. Res., 93*, 8869-8891, 1988.

King, N. E., P. Segall, and W. Prescott, Geodetic measurements near Parkfield, California, 1959-1984, *J. Geophys. Res., 92*, 2747-2766, 1987.

King, R. W., and Y. Bock, Documentation for the MIT GPS analysis software: GAMIT, version 9.3, Mass. Inst. of Technol., Cambridge, 1995.

Larson, K. M., and D. C. Agnew, Application of the Global Positioning System to crustal deformation measurement, 1, Precision and accuracy, *J. Geophys. Res., 96*, 16,547-16,565, 1991.

Li, V. C., and J. R. Rice, Crustal deformation in great California earthquake cycles, *J. Geophys. Res., 92*, 11,533-11,551, 1987.

Lisowski, M., J. C. Savage, and W. H. Prescott, The velocity field along the San Andreas fault in central and southern California, *J. Geophys. Res., 96*, 8369-8389, 1991.

Ma, C., J. W. Ryan, and D. S. Caprette, NASA space geodesy program–GSFC data analysis–1993, *NASA Tech. Memo., tm-104605*, June 1994.

Michelson, A. A., Measurement of the velocity of light between Mount Wilson and Mount San Antonio, *Astrophys. J., 65*, 1-22, 1927.

Morton, D. M., and J. C. Matti, The Cucamonga fault zone: Geological setting and Quaternary history, *U.S. Geol. Surv. Prof. Pap., 1339*, 179-203, 1987.

Namson, J. S., and T. L. Davis, Seismically active fold and thrust belt in the San Joaquin Valley, central California, *Geol. Soc. Am. Bull., 100*, 257-273, 1988.

Nur, A., and G. Mavko, Post-seismic viscoelastic rebound, *Science, 183*, 204-206, 1974.

Okada, Y., Surface deformation to shear and tensile faults in a half-space, *Bull. Seismol. Soc. Am., 75*, 1135-1154, 1985.

Okada, Y., Internal deformation due to shear and tensile faults in a half-space, *Bull. Seismol. Soc. Am., 82*, 1018-1040, 1992.

Pertersen, M. D., C. H. Cramer, W. A. Bryant, M. S. Reichle, and T. R. Toppozada, Preliminary seismic hazard assessment for Los Angeles, Ventura, and Orange counties, California, Affected by the 17 January 1994 Northridge earthquake, *Bull. Seismol. Soc. Am., 86*, No. 1B, S247-S261, 1996.

Prescott, W. H., An extension of Frank's method for obtaining crustal shear strains from survey data, *Bull. Seismol. Soc. Am., 66*, 1847-1853, 1976.

Rundle, J. B., and D. D. Jackson, A three-dimensional viscoelastic model of a strike slip fault, *Geophys. J. R. Astron. Soc., 49*, 575-591, 1977a.

Rundle, J. B., and D. D. Jackson, A viscoelastic relaxation model for post-seismic deformation from the San Francisco earthquake of 1906, *Pure Appl. Geophys., 115*, 401-411, 1977b.

Salyards, S. L., K. E. Sieh, and J. L. Kirschvink, Paleomagnetic measurement of nonbrittle coseismic deformation across the San Andreas fault at Pallett Creek, *J. Geophys. Res., 97*, 12,457-12,470, 1992.

Sauber, J., M. Lisowski, and S. C. Solomon, Geodetic measurement of deformation east of the San Andreas Fault in central California, in *Slow Deformation and Transmission of Stress in the Earth, Geophys. Monogr. Ser.*, vol. 49, edited by S. Cohen and P. Vanicek, pp. 71-86, AGU, Washington, D. C., 1989.

Sauber, J., W. Thatcher, S. C. Solomon, and M. Lisowski, Geodetic slip rate for the eastern California shear zone and the recurrence time of Mojave desert earthquakes, *Nature, 367*, 264-266, 1994.

Saucier, F., and E. Humphreys, Horizontal crustal deformation in southern California from joint models of geologic and very long baseline interferometry measurements, in *Contributions of Space Geodesy to Geodynamics: Crustal Dynamics, Geodyn. Ser.*, vol. 23, edited by D. E. Smith and D. L. Turcotte, pp. 139-176, AGU, Washington, D. C., 1993.

Savage, J. C., and M. Lisowski, Strain accumulation north of Los Angeles, California, as a function of time, 1977-1992, *Geophys. Res. Lett., 21*, 1173-1176, 1994.

Savage, J. C., and M. Lisowski, Geodetic monitoring of the southern San Andreas fault, California, 1980-1991, *J. Geophys. Res., 100*, 8185-8192, 1995a.

Savage, J. C., and M. Lisowski, Interseismic deformation along the San Andreas fault in southern California, *J. Geophys. Res., 100*, 12,703-12,717, 1995b.

Savage, J. C., and W. H. Prescott, Precision of Geodolite distance measurements for determining fault movements, *J. Geophys. Res., 78*, 6001-6008, 1973.

Savage, J. C., and W. H. Prescott, Asthenosphere readjustment and the earthquake cycle, *J. Geophys. Res., 83*, 3369-3376, 1978.

Savage, J. C., M. Lisowski, and W. H. Prescott, An apparent shear zone trending north-northwest across the Mojave desert into Owens valley, eastern California, *Geophys. Res. Lett., 17*, 2113-2116, 1990.

Shaw, J., and J. Suppe, Earthquake hazards of active blind-thrust faults under the central Los Angeles basin, California, *J. Geophys. Res., 101*, 8623-8642, 1996.

Shen, Z., Regional tectonic deformation in southern California, inferred from terrestrial geodesy and the Global Positioning System, Ph.D. thesis, 163 pp., Univ. of Calif., Los Angeles, 1991.

Sieh, K. E., and R. H. Jahns, Holocene activity of the San Andreas fault at Wallace Creek, California, *Geol. Soc. Am. Bull., 95*, 883-896, 1984.

Sieh, K., M. Stuiver, and D. Brillinger, A more precise chronology of earthquakes produced by the San Andreas fault in southern California, *J. Geophys. Res., 94*, 603-623, 1989.

Snay, R. A., M. W. Cline, C. R. Philipp, D. D. Jackson, Y. Feng, Z.-K. Shen, and M. Lisowski, Crustal velocity field near the Big Bend of California's San Andreas fault, *J. Geophys. Res., 101*, 3173-3185, 1996.

Sung, L.-Y., and D. D. Jackson, Crustal and uppermost mantle structure under southern California, *Bull. Seismol. Soc. Am., 82*, 934-961, 1992.

Svarc, J. L., J. C. Savage, M. Lisowski, and W. K. Gross, Strain accumulation 1973-1994 across the Nevada seismic zone, *Eos Trans. AGU, 75*(44), Fall Meet. Suppl., 179, 1994.

Thatcher, W., Nonlinear strain build-up and the earthquake cycle on the San Andreas fault, *J. Geophys. Res., 88*, 5893-5902, 1983.

Vincenty, T., A note on the reduction of measured distances to the ellipsoid, *Surv. Rev., 23*, 175, 1975.

Ward, S. N., A multidisciplinary approach to seismic hazard in southern California, *Bull. Seismol. Soc. Am., 84*, 1293-1309, 1994.

Webb, L. M., and H. Kanamori, Earthquake focal mechanisms in the eastern Transverse Ranges and San Emigdio Mountains, southern California and evidence for a regional decollement, *Bull. Seismol. Soc. Am., 75*, 737-757, 1985.

Weldon, R., and E. Humphreys, A kinematic model of southern California, *Tectonics, 5*, 22-48, 1986.

Wessel, P., and W. H. F. Smith, Free software helps map and display data, *Eos Trans. AGU, 72*, 441, 445-446, 1991.

Working Group on California Earthquake Probabilities, Probabilities of large earthquakes occurring in California on the San Andreas fault, *U.S. Geol. Surv. Open File Rep., 88-398*, 1988.

Working Group on California Earthquake Probabilities, Seismic hazards in southern California: Probable earthquakes, 1994-2024, *Bull. Seismol. Soc. Am., 85*, 379-439, 1995.

Wright, T., Geologic evolution of the petroleum basins of southern California, in *Petroleum Geology of Coastal Southern California*, edited by T. Wright and R. Heck, pp. 1-20, Pac. Sect. Am. Assoc. of Pet. Geol., Los Angeles, Calif., 1987.

Ziony, J. I., and R. F. Yerkes, Evaluating earthquake and surface-faulting potential, in *Evaluating Earthquake Hazards in the Los Angeles Region: An Earth-Science Perspective*, edited by J. I. Ziony, *U.S. Geol. Surv. Prof. Pap., 1360*, 43-91, 1985.

B. X. Ge, D. D. Jackson, and Z.-K. Shen, Department of Earth and Space Sciences, University of California, 3806 Geology, 595 Circle Drive, Los Angles, CA 90095-1567. (e-mail: zshen@hercules.ess.ucla.edu)

(Received October 6, 1995; revised June 19, 1996; accepted August 13, 1996.)